Science and Technology Facilities Council

Technical Report
STFC-TR-2026-016

In-situ mechanochemical synthesis for diffraction instruments

I da Silva, A Mortazavi,
M Perfecto-Irigaray

July 2026

Enquiries concerning this report should be addressed to:

RAL Library
STFC Rutherford Appleton Laboratory
Harwell Oxford
Didcot
OX11 0QX

Tel: +44(0)1235 445577
email: library@stfc.ac.uk

Science and Technology Facilities Council reports are available online at:
https://epubs.stfc.ac.uk

Accessibility: a Microsoft Word version of this document (for use with assistive technology) may be available on request.

DOI: 10.5286/stfctr.2026016

ISSN 2753-5797

STFC Author Identifiers (ORCIDs)

Author ORCIDs are provided where available.

Ivan Da Silva	0000-0002-4472-9675
Ali Mortazavi	0009-0004-2746-3125
Maite Perfecto-Irigaray	0000-0001-7228-9470

In-Situ Mechanochemical Synthesis for Diffraction Instruments

Ivan da Silva, Ali Mortazavi, Maite Perfecto-Irigaray

Abstract

Mechanochemical synthesis, in which a chemical reaction is driven by mechanical energy, is an increasingly popular synthetic approach used to prepare a wide range of materials, including inorganic (oxides, sulfides, nitrides, hydrides), organic (pharmaceutical co-crystals) and metal–organic compounds (metal–organic frameworks, MOFs). Mechanosynthesis can promote rapid reactions between solids with little or no solvent, requiring shorter reaction times and often with improved yield and purity when compared to wet synthesis routes. However, the mechanisms that govern mechanochemical reactions remain poorly understood. This is largely due to the difficulty of analysing powder mixtures during milling: mechanistic studies typically rely on periodically interrupting the milling process to sample the mixture. Interrupting the experiment reduces reliability because sampling can alter the product (for example, through temperature changes or solvent loss), and it makes detection of short-lived intermediates difficult. Here we present the design and development of an equipment to enable *in-situ* neutron diffraction studies of mechanochemical reactions.

1. Aims of the project

The project is structured around two core objectives, each addressing a critical gap in current mechanochemical research capabilities and aiming to establish a robust platform for real-time structural studies during milling.

1.1. Develop and build a ball-mill mechanochemical reactor for *in-situ* neutron diffraction studies on GEM instrument

At present, no ball-mill reactors exist that are compatible with *in-situ* neutron diffraction experiments at major neutron facilities. Developing such a device therefore represents a significant technological and scientific advance. The first objective focuses on the design and construction of a bespoke ball-mill reactor tailored to the operational constraints and geometric requirements of the GEM instrument.

The reactor must allow efficient transmission of neutrons through the milling chamber while maintaining mechanical robustness and safe operation under continuous milling conditions.

A key design feature will be the ability to perform mechanochemical reactions under controlled gas atmospheres (e.g., N_2, Ar), enabling the synthesis of air-sensitive materials such as nitrides and hydrides. The high penetration depth of neutrons makes it possible to collect diffraction data directly from inside the vessel during milling, providing unprecedented access to reaction pathways, phase evolution and intermediate species.

Once constructed, the reactor will undergo initial beamline testing using *ex-situ* prepared reference materials. These tests will assess neutron transparency, background scattering, sample environment stability and the overall quality of diffraction data obtained during operation.

1.2. Validate the mechanochemical reactor for the synthesis of representative functional materials

The second objective aims to demonstrate the practical utility and reliability of the newly developed reactor. Prior to beamline deployment, off-beamline testing will be carried out to evaluate the mechanical performance, milling efficiency and reproducibility of the device. Reference materials of diverse chemical nature—spanning inorganic, metal–organic and organic systems—will be synthesised using established mechanochemical protocols reported in the literature.

Following successful off-beamline validation, the reactor will be used for *in-situ* synthesis experiments on GEM. Neutron powder diffraction data collected during milling will allow real-time monitoring of phase evolution, enabling structural analysis of reactants, intermediates and final products. This final stage will confirm the reactor's suitability for mechanistic studies and establish it as a functional tool for future research into mechanochemical processes.

2. Introduction to the techniques

2.1. Mechanochemistry

Mechanochemistry refers to chemical reactions—typically involving solid reagents—that are initiated or accelerated by the application of mechanical energy, for example through grinding in ball mills.[1] This field has gained substantial momentum in materials science and technology because it enables rapid, quantitative transformations between solids, often without added solvent or using only minimal solvent quantities. Mechanochemical methods have proven not only effective but frequently advantageous for synthesising a wide variety of functional materials, including advanced inorganic compounds (alloys, ceramics, nanoparticles), pharmaceutical products, composites, and metal–organic materials.[2,3]

The heavy dependence of traditional synthetic chemistry on solvents is increasingly recognised as unsustainable. Solvents consume significant fossil-derived resources, pose environmental and human-health hazards, and require energy-intensive production, purification and recycling processes that contribute to greenhouse-gas emissions.

Mechanochemistry offers a compelling alternative: it reduces solvent use, lowers energy demands, and often simplifies reaction workflows. As a result, mechanochemical synthesis aligns strongly with the principles of green chemistry and sustainable materials development.

Despite these advantages, the fundamental mechanisms governing mechanochemical reactions remain poorly understood. Reaction pathways, intermediate species, and kinetic profiles are difficult to probe because milling environments are dynamic, heterogeneous, and typically inaccessible to conventional analytical techniques. Interrupting milling to extract samples can alter reaction conditions, obscure transient intermediates, and reduce the reliability of mechanistic interpretations. Consequently, *in-situ* measurement methodologies are attracting growing interest.[4] Real-time structural probes—particularly neutron-based techniques—offer a powerful route to elucidate how mechanochemical reactions proceed at the atomic scale.

2.2. Neutron Powder Diffraction

The *in-situ* mechanochemical reactor developed in this project is designed for use on GEM, a time-of-flight (TOF) neutron powder diffraction (NPD) instrument located at Target Station 1 of the ISIS Neutron and Muon Source. NPD provides detailed insight into the atomic structure of materials by measuring neutrons that are elastically scattered from the sample—meaning the neutrons retain their energy during the scattering event.

For polycrystalline powders, where each crystallite exhibits long-range atomic order, the scattered neutrons interfere to produce Bragg reflections, observed as peaks in the measured scattering intensity as a function of TOF. Analysis of these reflections yields precise information about the crystal structure, including lattice parameters, atomic positions, phase composition and structural evolution under varying conditions.

When the sample contains multiple phases, the recorded diffraction pattern represents the weighted sum of the individual diffraction patterns of each component. Because the intensity contribution of each phase scales with its weight fraction, NPD enables quantitative phase analysis. This capability is particularly valuable for mechanochemical studies: by collecting diffraction data *in-situ* during milling, NPD can track the consumption of reactants, the appearance and disappearance of intermediates, and the formation of final products in real time.

The high penetration depth of neutrons makes them uniquely suited for probing materials inside sealed or opaque milling vessels, allowing structural information to be obtained without interrupting the reaction. This makes NPD an ideal technique for advancing mechanistic understanding of mechanochemical processes and for validating the performance of newly developed mechanochemical reactors.

3. Mechanochemical reactor design

Procurement and Customisation of the Base Unit

For this project, a customised version of the Fritsch Pulverisette 23 ball mill was procured. In this bespoke configuration, the standard on-device control panel and display have been detached from the milling body and mounted on a remote unit connected via a cable. This modification allows the milling mechanism to be integrated into the GEM sample tank while keeping the control electronics safely outside the instrument's restricted area.

The standard Pulverisette 23 configuration and the customised remote-panel version are shown in Figure 1.

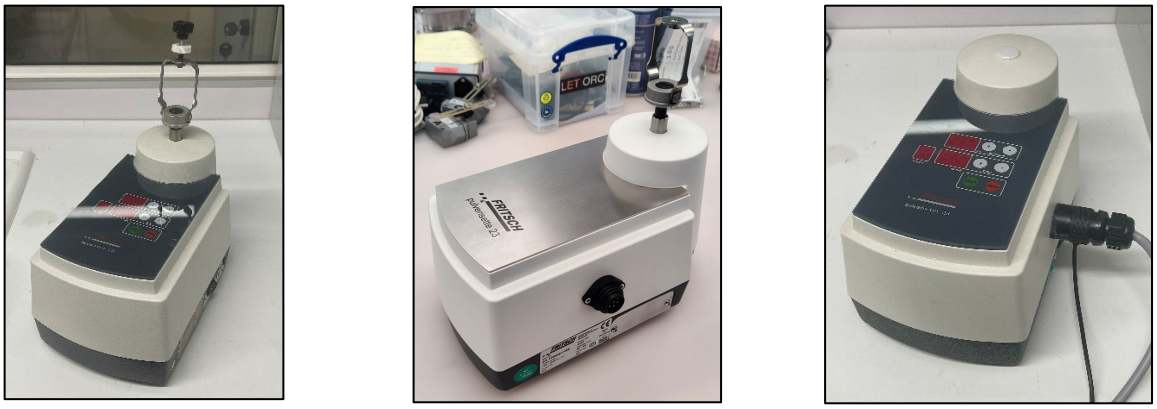

Figure 1. Standard Pulverisette 23 ball-mill (left), and the bespoke version where the ball-mill mechanism (centre) has been detached from the control panel (right).

Principle of Operation

The Pulverisette 23 operates using a piston-engine-style mechanism driven by a 24 VDC, 3 A motor. The motor actuates an eccentric crank pin connected to a conrod and piston assembly, generating a reciprocating motion. The milling capsule is mounted at the end of the piston and secured using a screw-fastened cage. This securing screw both holds the capsule in position and keeps it closed, as the capsule itself has no integrated locking mechanism. Key operational parameters include a stroke length of 9 mm and selectable reciprocation speed up to 50 Hz (50 rpm equivalent for the motor).

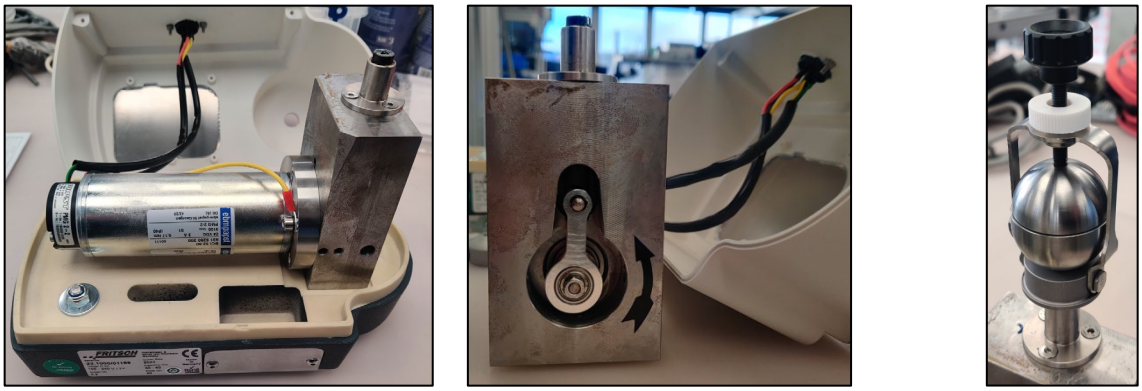

Figure 2. Images of Pulverisette 23 ball-mill with top case removed (left), reciprocating mechanism (centre) and reactor held in its operational position (right).

Integration into the GEM Instrument

The core engineering task is to remove the external casing of the ball mill and mount the milling mechanism upside-down onto a Tomkinson flange via a dedicated support plate. This configuration allows the reactor to be introduced directly into the GEM sample tank while maintaining alignment with the neutron beam.

Because the ball mill must remain permanently mounted to the Tomkinson flange during beamline operation, a second Pulverisette 23 unit was purchased for off-line laboratory testing and development work.

Mechanical Design Overview

The inverted ball mill is attached to a primary mounting plate, which is connected to a secondary support plate through four anti-vibration mounts. These mounts isolate the reciprocating motion from the rest of the assembly, reducing mechanical noise and protecting the GEM instrument components. The support plate is connected to a bespoke Tomkinson flange using four structural rods. An aluminium protective can is installed on the support plate to shield the GEM oscillating radial collimator in the event that the milling capsule becomes loose during operation. The protective can includes two neutron-transparent windows (beam-in and beam-out), each covered with vanadium foil to minimise background scattering. The Tomkinson flange incorporates integrated lifting points for safe handling and installation and three KF50 ports for vacuum connections and electrical feedthroughs.

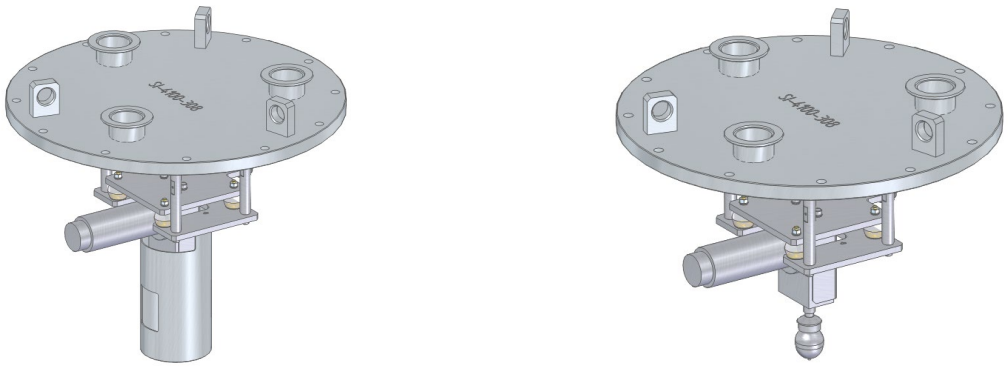

Figure 3. Engineering drawings of ball mill system with (left) and without protecting “pot” (right).

Storage and Transportation System

A dedicated storage and transportation trolley was designed using ITEM aluminium extrusion profiles. The trolley includes a rubberised top surface to prevent damage to the Tomkinson flange and plastic corner guides to ensure the flange remains centred and stable during transport.

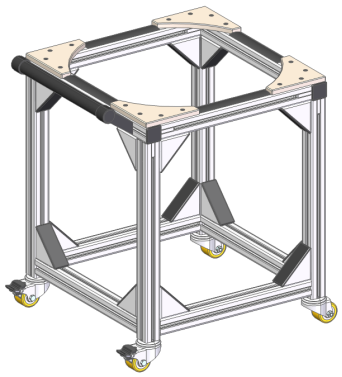

Figure 4. Engineering drawing of storage / transportation trolley.

Figure 5. Photographs of the final modified ball mill, sitting on the storage / transportation trolley (left), and being craned from the trolley into the GEM instrument for conducting neutron powder diffraction experiments (centre and right).

4. GEM neutron diffraction tests

The following section presents the experimental results obtained from a series of neutron powder diffraction measurements carried out on the GEM instrument using the modified ball-mill reactor described previously. These measurements constitute the first validation experiments performed with the adapted mechanochemical setup under real beamline conditions.

To facilitate direct comparison between datasets collected from different GEM detector banks, all diffraction patterns are displayed as a function of d-spacing. Representing the data in d-spacing units allows structural features to be aligned across banks with different scattering-angle geometries, enabling more robust interpretation of phase evolution and peak behaviour during milling.

All neutron diffraction datasets included in this report have undergone a standardised normalisation procedure to ensure quantitative comparability:

- Beam-current normalisation: each dataset has been normalised to the total proton beam current delivered during acquisition. This correction accounts for variations in effective counting time and ensures that intensity differences reflect sample behaviour rather than fluctuations in source output.
- Moderator spectrum normalisation: the diffraction intensity has also been normalised against data collected from an 8-mm-diameter vanadium rod. Vanadium provides a featureless, nearly flat scattering profile and is routinely used to characterise the incident neutron energy distribution from the liquid CH_4 moderator. Normalising against this reference removes spectral variations associated with the moderator and allows intensities to be compared directly across different experimental runs.

Together, these corrections ensure that the diffraction patterns presented in this document reflect intrinsic sample behaviour and can be reliably used for assessing reactor performance, monitoring reaction progress, and evaluating the suitability of the system for future *in-situ* mechanochemical studies.

4.1. Characterisation of empty reactors

This first section presents the neutron diffraction measurements acquired from the different reactor configurations evaluated throughout the project, including both commercial vessels and bespoke designs developed specifically for the ball-mill. The aim of this preliminary study is to characterise the intrinsic diffraction profile and background signal associated with each reactor, establishing their suitability for *in-situ* measurements on GEM.

A systematic comparison of reactor components is essential because the choice of sample holder can significantly influence data quality. Factors such as neutron absorption, incoherent scattering, and background contributions can affect peak intensities, baseline stability and overall signal-to-noise ratio. By quantifying these effects for each design, we can identify the most appropriate configurations for subsequent mechanochemical experiments and ensure that structural features arising from the sample are not obscured by artefacts from the reactor material.

The results presented in the following subsections therefore provide a baseline assessment of the neutron transparency of each holder, the magnitude and profile of background scattering, the presence of spurious features or parasitic peaks, and the overall compatibility of each design with GEM's detector geometry and beam characteristics.

This characterisation step is a critical precursor to *in-situ* mechanochemical studies, ensuring that the reactor and its associated components meet the performance requirements for reliable structural analysis under dynamic milling conditions.

4.1.1. ZrO_2 spherical reactor (as received from the company):

Figure 6. Photo of the ZrO2 spherical reactor (15 mL volume capacity) and milling balls (10 mm diameter), as received from the Fritsch company.

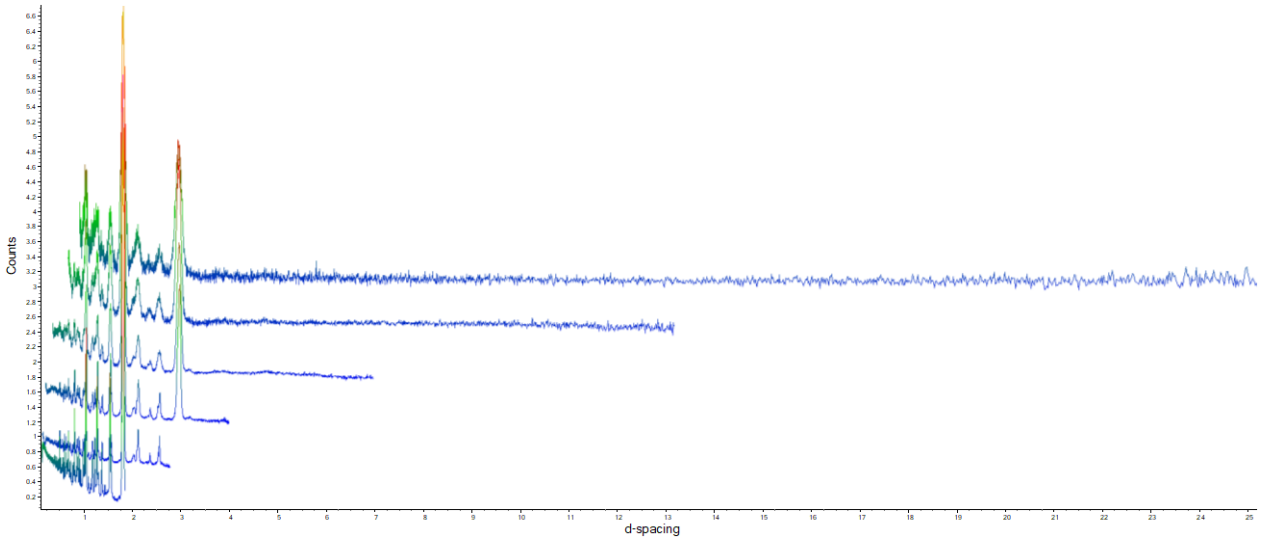

Figure 7. Collected GEM diffraction data, showing detector banks from #1 (top) to #6 (bottom). Diffraction patterns have been shifted along the Y-axis for clarity

The data shows many reflections coming from the reactor and milling balls, at *d*-spacings below ~3 Å. This would be detrimental to get quality data from a powder sample loaded inside the reactor, as its diffraction reflections would be overlapping those coming from the reactor. The data from the sample would only be good at *d*-spacings above ~3 Å.

4.1.2. Stainless-steel spherical reactor (as received from the company)

Figure 8. Photo of the stainless-steel spherical reactors (15 and 10 mL volume capacity) and milling balls (10 and 5 mm diameter), as received from the Fritsch company.

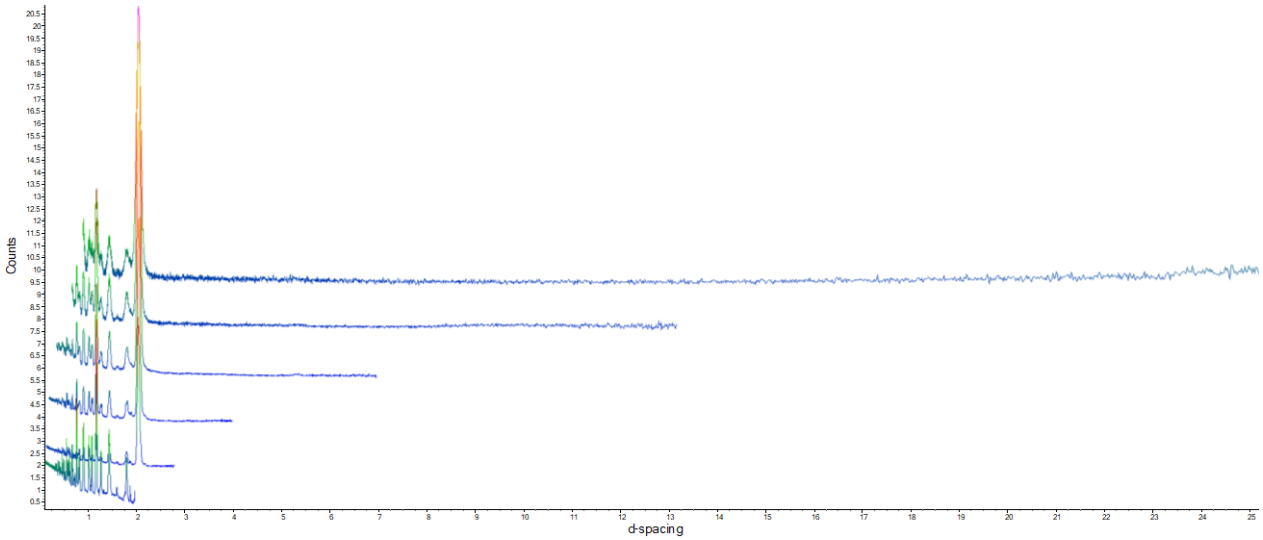

Figure 9. Collected GEM diffraction data, showing detector banks from #1 (top) to #6 (bottom). Diffraction patterns have been shifted along the Y-axis for clarity

The diffraction data shows many reflections coming from the reactor and milling balls, at d-spacings below ~2 Å.

The limiting *d*-spacing value is slightly lower than for the case of ZrO_2, which is advantageous (there would be more *d*-spacing range for detecting possible reflections coming from the powder sample under study).

However, the intensity contribution from the stainless-steel reactor is much higher than the case of the ZrO_2 one (the sample reflections overlapping those from the reactor would be more difficult to be observed).

4.1.3. Aluminium reactor (spherical bespoke design based on the stainless steel one)

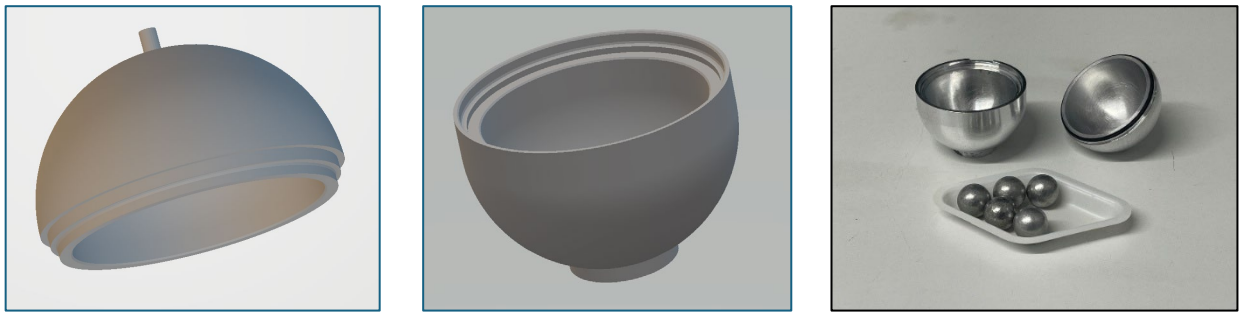

Figure 10. Images of the 3D engineering design (left and centre) and photo of the mechanized aluminium spherical reactors and milling balls (10 mm diameter).

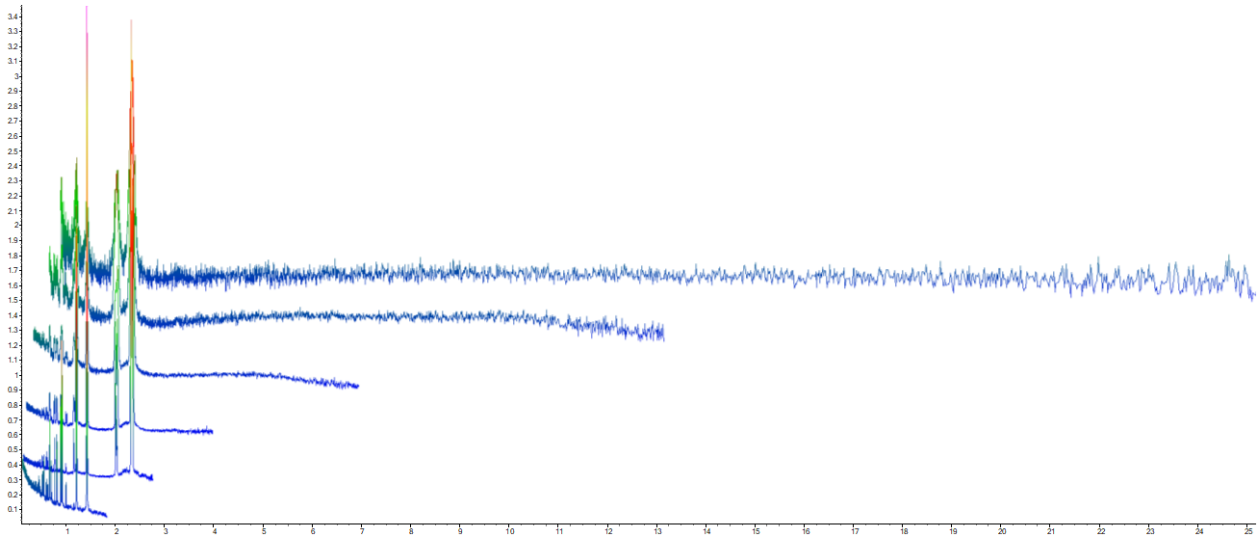

Figure 11. Collected GEM diffraction data, showing detector banks from #1 (top) to #6 (bottom). Diffraction patterns have been shifted along the Y-axis for clarity

The diffraction patterns still shows numerous reflections arising from the aluminium reactor and the milling balls, with a limiting *d*-spacing range that lies between those characteristic of the ZrO_2 and stainless-steel reactors. However, the reflections coming from the aluminium are more widely spaced, which is advantageous: the increased separation provides a broader low-*d*-spacing window in which potential sample reflections can be observed without overlapping those from the reactor.

A further positive aspect is that both the intensity of the aluminium reflections and the associated background contributions are significantly lower than those produced by the ZrO_2 and stainless-steel reactors. This reduction in scattering enhances overall data quality and improves the prospects for extracting meaningful structural information from powder samples loaded inside the aluminium reactor.

4.1.4. PTFE reactor (cylindrical bespoke design)

A new reactor has been designed with a cylindrical geometry, which is better suited to the GEM instrument than the previous spherical design. This improvement stems from the rectangular cross section of the incoming neutron beam: in the spherical reactor, significant lateral regions remain “dead volume” that cannot be illuminated. In contrast, the cylindrical geometry allows the beam to fully cover the sample region, maximising the illuminated volume and improving data collection efficiency. Figure 12 shows the final concept for the PTFE reactor, which is straightforward to machine and ensures that most of the sample is visible through the PTFE walls. The reactor consists of three components: two stainless steel end pieces (top and bottom) and an interchangeable PTFE central section. Two versions of this PTFE insert were fabricated, with wall thicknesses of 0.5 mm and 1 mm, enabling assessment of neutron transparency, mechanical stability, and background contributions as a function of wall thickness.

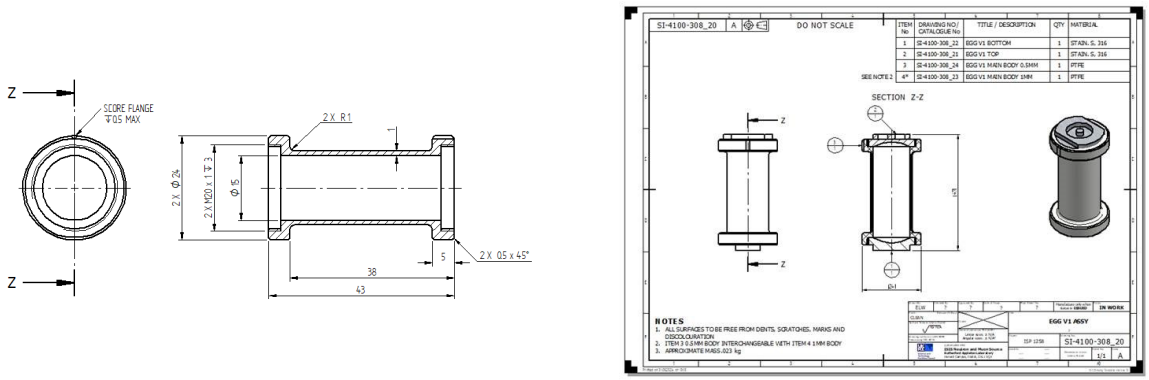

Figure 12. Bespoke cylindrical PTFE ball mill reactor engineering drawings

The sample is loaded into the reactor together with the grinding balls, after which the three components are screwed together. The final reactor configuration was designed to fit securely into the ball-mill holding arc and to be locked in place using the same screw mechanism employed for the spherical reactors.

Figure 13. Sample leaking issues (highlighted with yellow dotted circle) encountered with the first PTFE ball mill reactor version.

For the first design iteration, issues arose in off-line synthesis optimisation experiments: sample leakage occurred at the interface between the reactor body and the lid (see Figure 13), particularly during liquid-assisted grinding (LAG) reactions. To address this, an improved version incorporated a rubber O-ring (shown in green in Figure 14), providing a more reliable seal and preventing material loss during milling.

Figure 14. Final design drawings (left) and photo of the PTFE cylindrical reactors (7 mL volume capacity) and milling balls (8 and 5 mm diameter) (right).

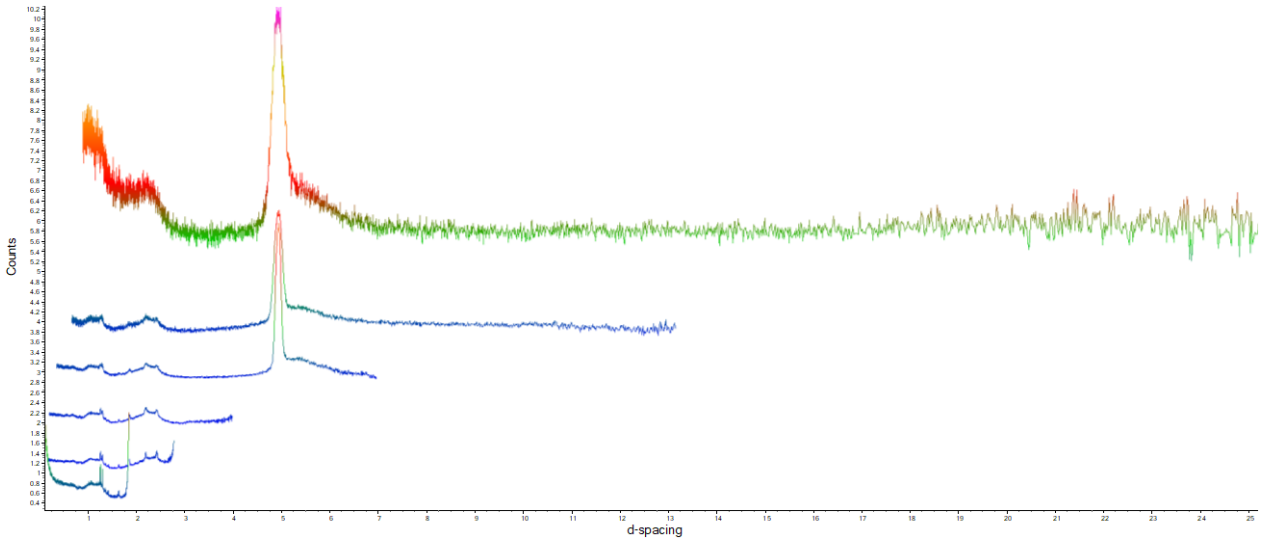

Figure 15. Collected GEM diffraction data, showing detector banks from #1 (top) to #6 (bottom). Diffraction patterns have been shifted along the Y-axis for clarity

Diffraction measurements show that the PTFE reactor and milling balls contribute only a small number of reflections, owing to the low crystallinity of PTFE. This is advantageous, as reflections from a powder sample inside the reactor should remain visible. However, the background level is relatively high, which represents a significant drawback for high-quality diffraction analysis.

A further limitation emerged during repeated synthesis trials: after prolonged milling times, the PTFE reactors exhibited noticeable deformation (see Figure 16). This mechanical instability restricts their long-term usability and highlights the need for alternative materials or reinforced geometries for sustained mechanochemical operation.

Figure 16. Different instances of the deforming issue encountered after repeated use of the PTFE ball mill reactor.

4.1.5. Aluminium reactor (cylindrical design, based on PTFE reactor)

This reactor follows the same overall design as the PTFE version, but with the main body machined from aluminium and stainless-steel lids. As in the PTFE design, a rubber O-ring is incorporated at each end of the assembly to ensure a reliable seal and prevent powder leakage during milling.

Figure 17. Photograph of the aluminium cylindrical reactors (7 mL volume capacity).

4.1.6. Vanadium reactor, based on a standard ISIS vanadium sample holder

Among the possible materials for the reactor body, vanadium is the most suitable from a neutron-diffraction perspective, as it is effectively transparent to neutrons. However, manufacturing a bespoke vanadium reactor analogous to the PTFE and aluminium cylindrical designs would be quite expensive. For this reason, we pursued an alternative approach: constructing a ball-mill reactor using one of the standard vanadium cans employed at ISIS, and adapting the lid to define an appropriate internal sample volume. As with the cylindrical reactor concept, the sample and milling balls are placed inside the vanadium can, after which the lid and can are screwed together. No O-ring is used in this assembly; instead, indium wire can be inserted between the lid and the can to provide a reliable seal when an inert atmosphere is required.

The extended lid design leaves a 35 mm sample space at the bottom of the vanadium can, ensuring that most of the sample remains visible to the neutron beam while the reactor is in motion. The resulting sample volume is approximately 3 mL for a 10 mm-diameter can and 6 mL for a 15 mm-diameter can. Unlike the spherical and cylindrical reactors, these vanadium-can reactors cannot be mounted in the ball-mill metal arc. The arc must therefore be removed, and the reactor is attached directly to the ball-mill piston. The fit between the lid extension and the can is constrained by the can–lid interface, producing a 1.32 mm gap between the extension and the can wall. Although this gap is smaller than the diameter of the milling balls—preventing them from becoming trapped—there is still a risk that powder may migrate into this space, reducing the amount of sample visible to the beam.

Finally, the ISIS workshop successfully machined a small set of vanadium milling balls for this project, enabling fully vanadium-based milling assemblies with minimal unwanted scattering.

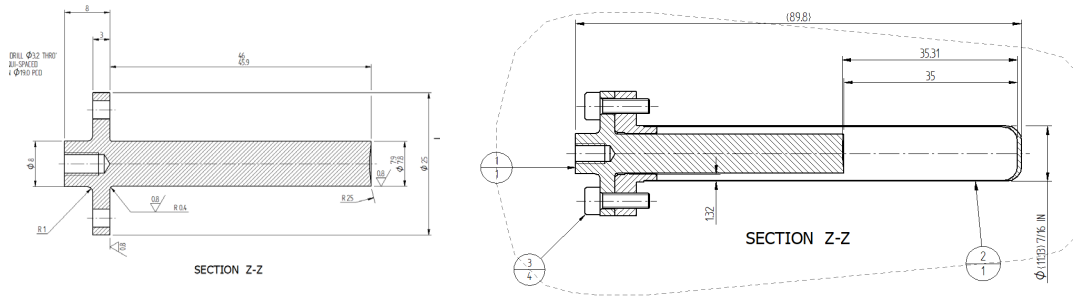

Figure 18. Bespoke stainless-steel lid (left) for the ISIS standard vanadium can and assembly (right) drawings.

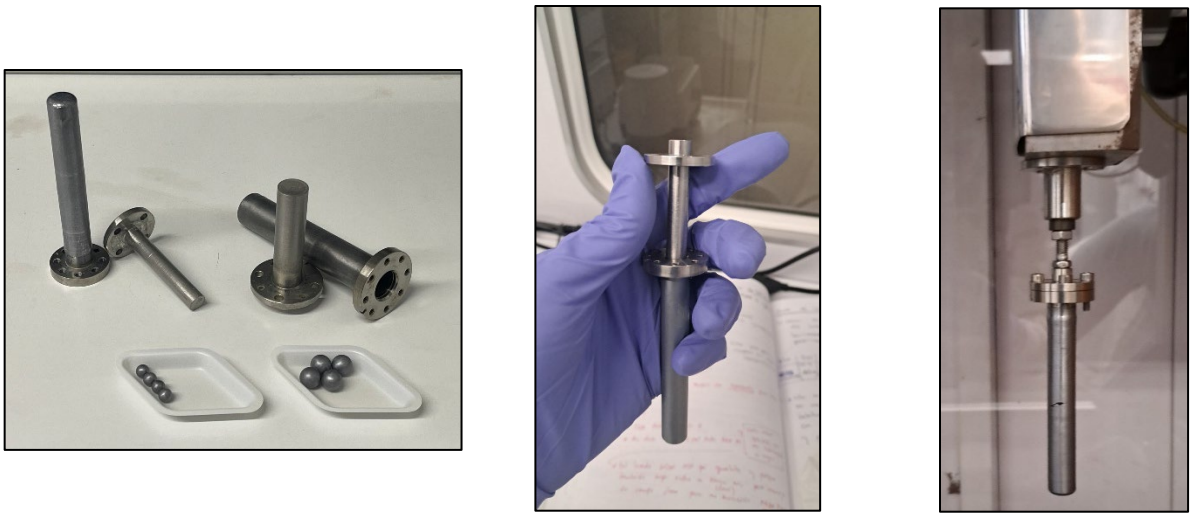

Figure 19. Photograph of the vanadium cans, modified lids and milling balls (8 and 5 mm diameter) (left), insertion of lid in the can (centre), and final assembly attached to ball mill.

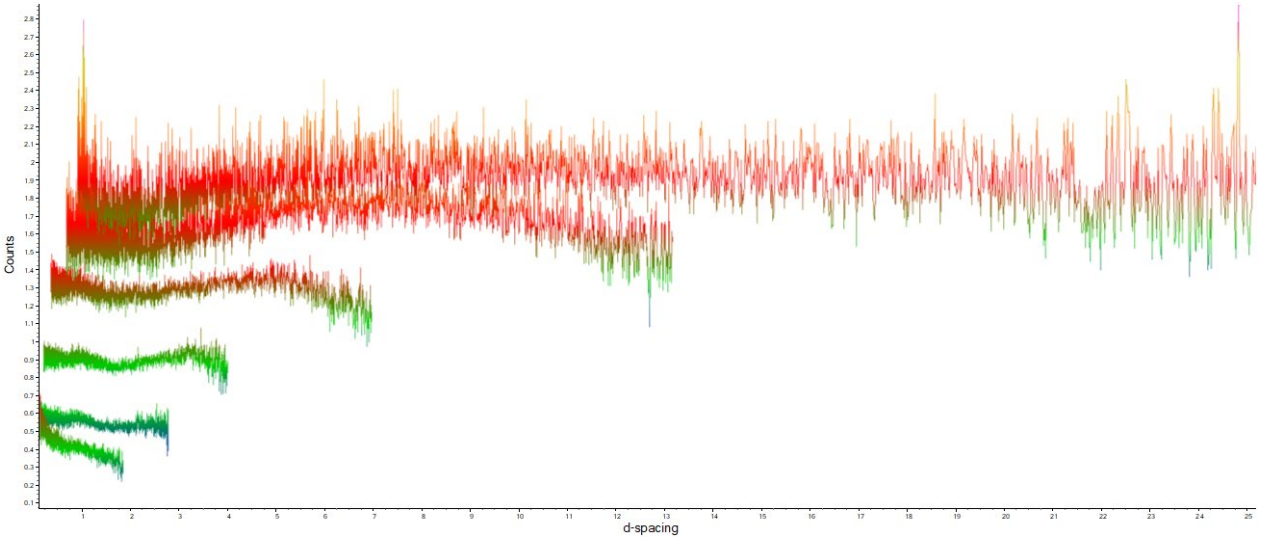

Figure 20. Collected GEM diffraction data, showing detector banks from #1 (top) to #6 (bottom)). Diffraction patterns have been shifted along the Y-axis for clarity.

As expected, the vanadium reactor and the vanadium milling balls produce no observable Bragg reflections, since vanadium is effectively transparent to neutrons. This represents the optimal outcome in terms of reactor-material performance: all diffraction features arising from a sample loaded inside the reactor should be fully visible in the pattern, without reactor peak overlap or masking from its assembly.

4.1.7. Summary of GEM data from all the tested materials used for reactors

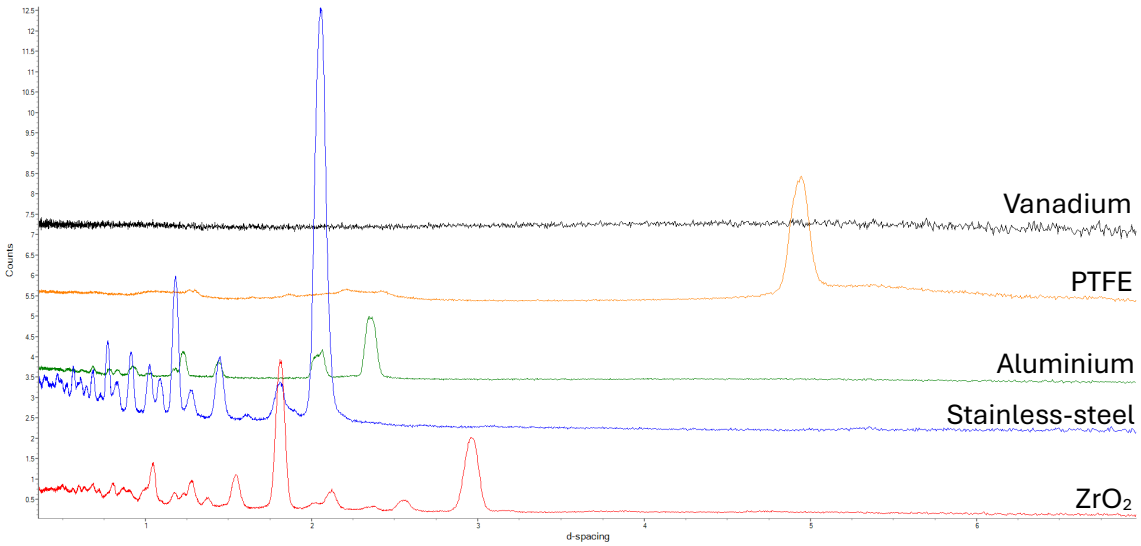

Figure 21. Bank #3 detector data, collected on GEM for the different empty reactors. Diffraction patterns have been shifted along the Y-axis for better visualization of contribution reflections.

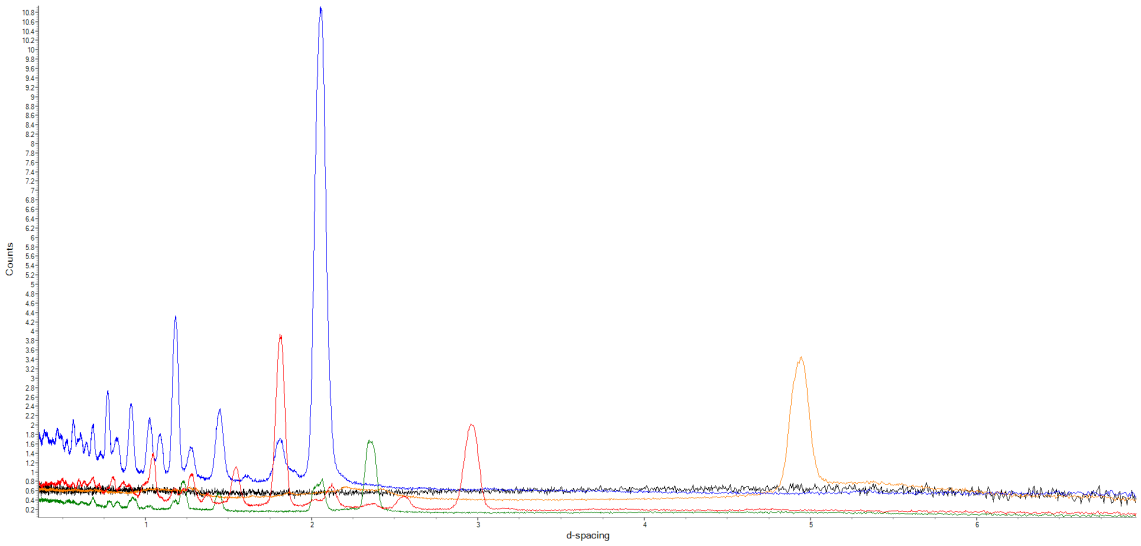

Figure 22. Bank #3 detector data collected on GEM for the various empty reactors. No shift along the Y-axis has been applied on this plot, allowing direct comparison of background levels. Line colours follow the same assignment used in figure 21.

Although aluminium provides the lowest background signal among the reactor materials tested, vanadium delivers a nearly flat background with no detectable diffraction peaks, highlighting its exceptional suitability for neutron-based mechanochemical studies. This behaviour shows the high potential of vanadium for use in both reactor bodies and milling media, as it enables unobstructed observation of all sample-derived reflections in the diffraction pattern.

4.1.8. Effect of vacuum on the diffraction data

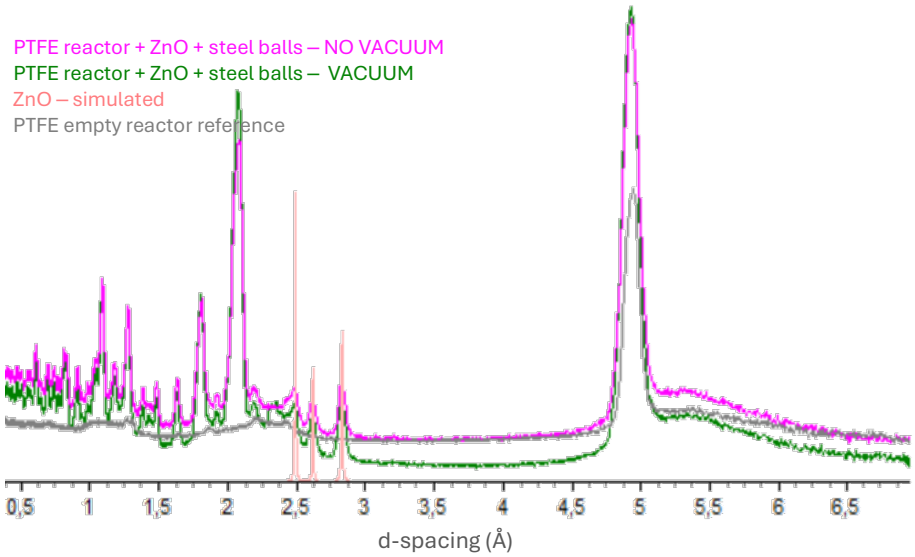

Figure 23. Bank #3 detector data collected on GEM for a PTFE reactor (0.5mm wall thickness), half-filled with ZnO powder sample and steel balls, measured both with vacuum applied in the GEM sample tank (green line) and under ambient air (magenta line). The empty reactor PTFE signal (grey line) and the simulated ZnO diffraction

pattern (pink line) are included for comparison. No vertical offset has been applied, allowing direct assessment of background levels and sample-derived intensities.

Although applying vacuum in the GEM tank yields a slightly lower background, the data collected under ambient air still exhibit acceptable quality. Importantly, the reduced intensity observed for powder samples (e.g., ZnO) does not appear to originate from the tank atmosphere, as shown by the comparison with the stainless-steel balls + PTFE reactor configuration.

4.1.9. Effect of aluminium safety "pot" on the diffraction data

An aluminium safety pot is used when operating the ball mill inside the GEM sample tank. It encloses the reactor and protects the oscillating radial collimator system from accidental impacts should the reactor detach or fall during milling. It also prevents the reactor from becoming lost inside the tank.

Figure 24. Engineering drawing showing the safety aluminium pot (left), and photos of the actual version (centre and right), where the incoming/outcoming beam windows can be seen covered with vanadium foil.

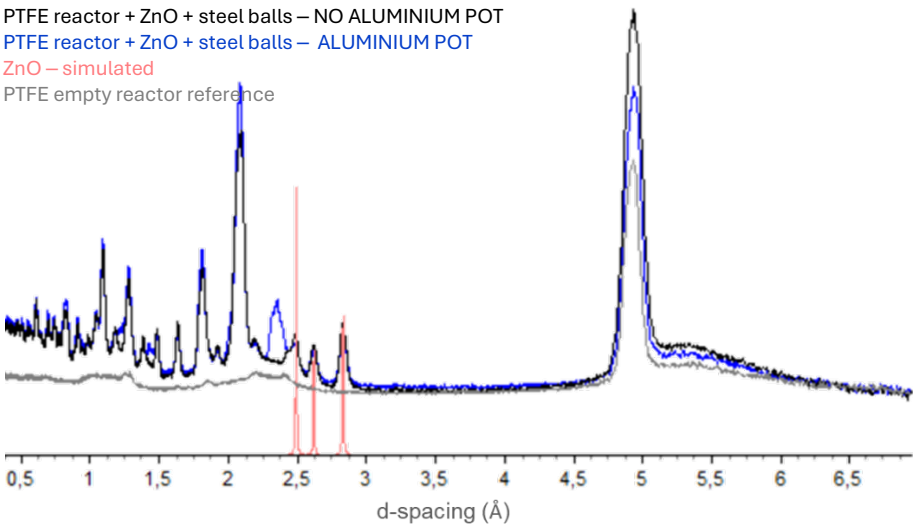

Figure 25. Bank #3 detector data, collected on GEM for a PTFE reactor (0.5mm wall thick), half-filled with ZnO powder sample and steel balls, with (blue line) and without (black line) the aluminium safety "pot". The empty

PTFE reactor signal (grey line) and the simulated ZnO diffraction pattern (pink line) are also shown for comparison.

On figure 25, a small contribution from aluminium diffraction can be observed on the blue curve. This indicates that the safety pot was not perfectly aligned vertically, causing the neutron beam to strike the edge of the pot's incoming/outgoing windows. When correctly centred on the vanadium window, however, the aluminium pot does not degrade the quality of the collected diffraction data. The results demonstrate that safe operation with the aluminium protection pot is fully compatible with high-quality measurements, provided the beam alignment is properly maintained.

4.2. *In-situ* mechanochemical reactions

In this section, the neutron-diffraction results obtained from the various *in-situ* mechanosynthesis trials carried out on GEM are presented. The experiments are organised following the same structure used in the Empty reactors section, maintaining a consistent ordering based on the reactor material employed. For each synthesis trial, diffraction data from selected GEM detector banks—covering different d-spacing ranges—are shown as a function of milling time to illustrate reaction progress and phase evolution.

Where applicable, Rietveld refinements have been performed using Topas Academic v6[6], enabling quantitative assessment of phase fractions and structural parameters throughout the mechanochemical reactions.

Synthesis reaction	Reactor / balls material
ZnO + 2-methylimidazole (mim) ⟶ ZIF-8 metal-organic-framework; LAG (liquid assisted grinding) with DMF	Stainless steel (spherical reactor)

Figure 26 shows the GEM *in-situ* data from the ZIF-8 synthesis reaction as a function of time, using a spherical stainless-steel reactor and balls. Apart from the very intense stainless-steel diffraction peaks, some very low-intensity diffraction peaks from the target compound are observable.

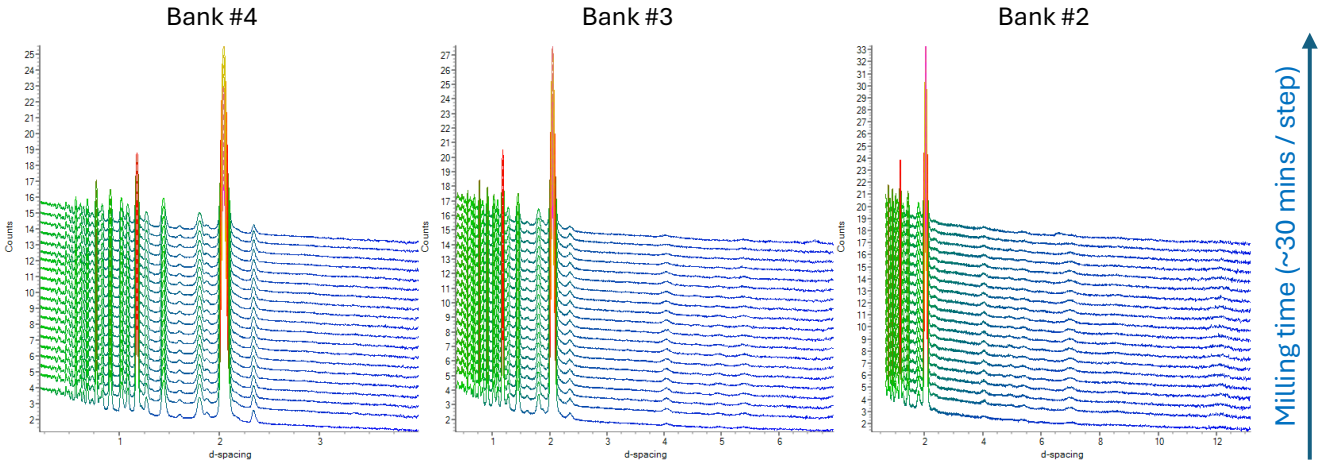

Figure 26. *In-situ* diffraction data, collected during mechanosynthesis of ZIF-8 material, for selected GEM detector banks. An offset has been applied along Y axis for better visualisation.

Figure 27 shows the Rietveld refinement result from a quantitative analysis of ZIF-8 and starting reactants, on the last mechanosynthesis process step, using only the experimental data ranges without contribution from the reactor and balls. It shows that a yield of almost 90% of ZIF-8 compound was obtained; however, the reaction took place too quickly relative to the data collection step-time in order to be monitored, while the diffraction intensity contribution from the powder sample is too low to offer reliable estimations of phase weight-percentages.

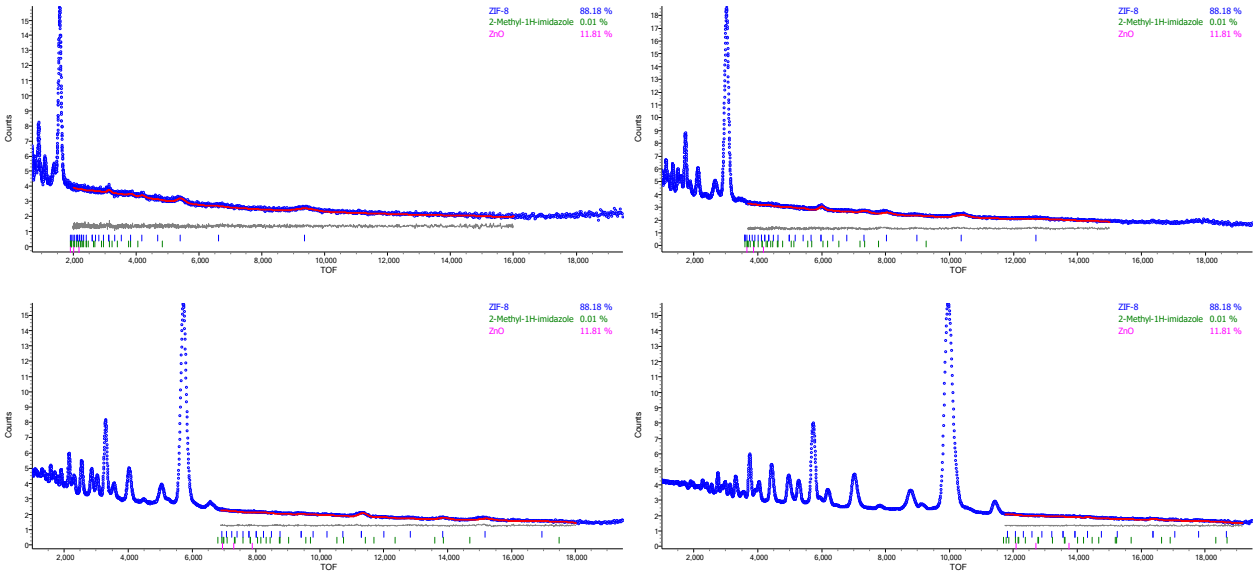

Figure 27. Rietveld refinement result plots for detector banks #1 to #4 (left to right and top to bottom), using the last collected dataset during *in-situ* mechanosynthesis of ZIF-8 material.

Synthesis reaction	Reactor / balls material
ZnO + 2,5-dihydroxyterephthalic acid → MOF-74 metal-organic-framework; LAG (liquid assisted grinding) with DMF	Aluminium (spherical reactor)

Figure 28 shows the GEM *in-situ* data from the MOF-74 synthesis reaction as a function of time, using a spherical aluminium reactor and balls. Apart from the very intense aluminium diffraction peaks, some low-intensity diffraction peaks from the starting and target compounds are observable.

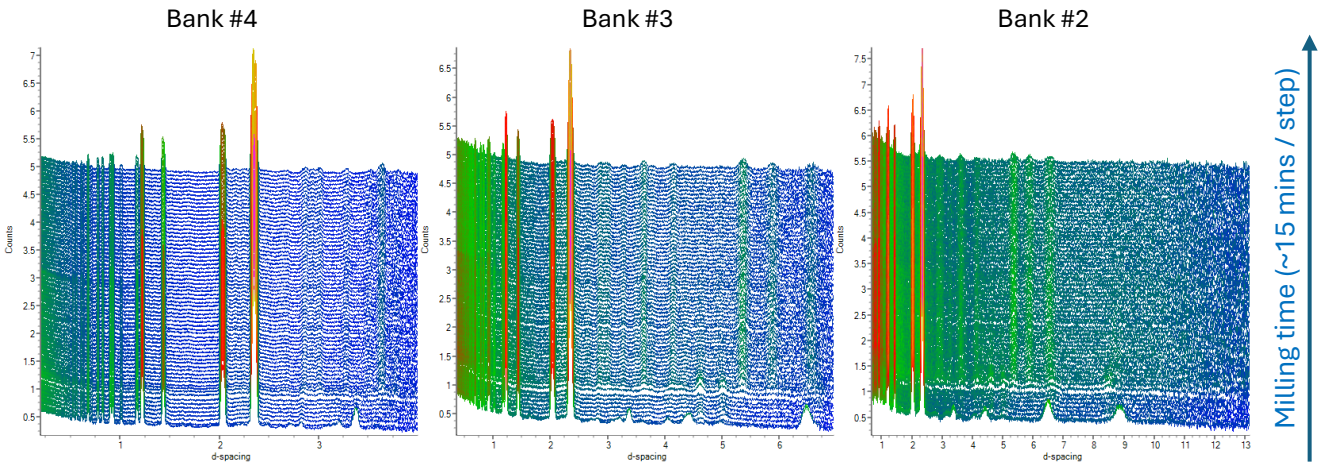

Figure 28. *In-situ* diffraction data, collected during mechanosynthesis of MOF-74 material, for selected GEM detector banks. An offset has been applied along Y axis for better visualisation.

A reaction is clearly initiated within the first few minutes of ball milling; however, the available time resolution and peak definition are insufficient to identify the transient intermediate phases with confidence. Beyond this initial period, the reaction appears to stall, with no significant further evolution observed in the diffraction patterns.

Figure 29 shows the Rietveld refinement result using the final MOF-74 crystal structure, on the last mechanosynthesis process step, using only the experimental data ranges without contribution from the reactor and balls (for bank #4 this range has been extended, but aluminium peaks contribution has been excluded from the refinement). It shows that the final MOF-74 compound has been successfully obtained.

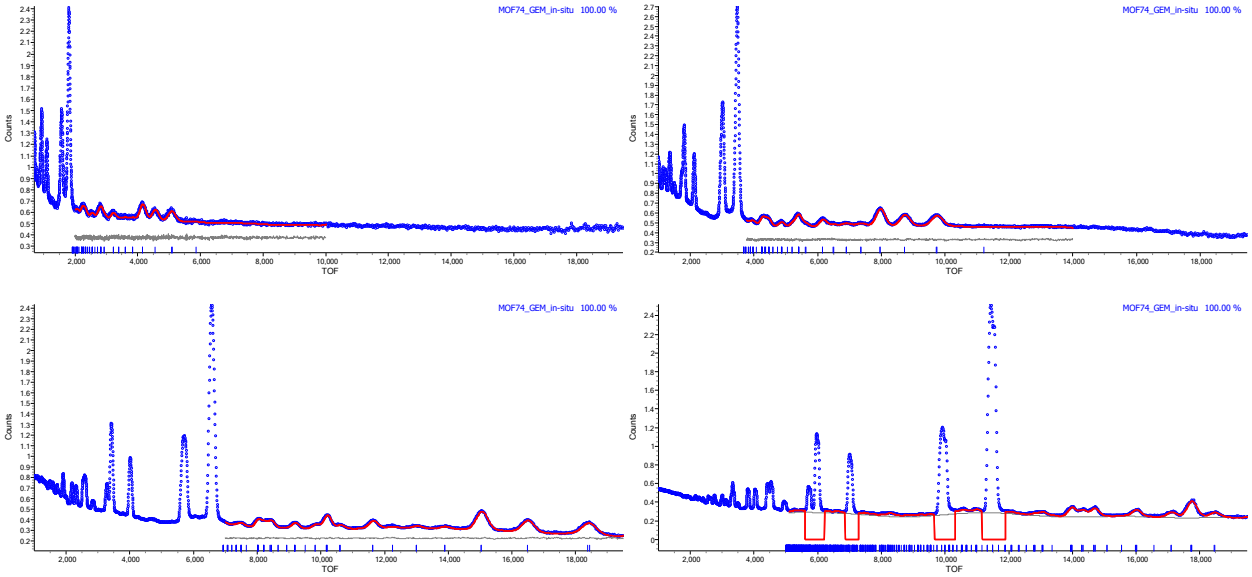

Figure 29. Rietveld refinement result plots for detector banks #1 to #4 (left to right and top to bottom), using the last collected dataset during *in-situ* mechanosynthesis of MOF-74 material.

A sequential Rietveld refinement was performed across all the measurement steps, and the resulting wt% evolution of the starting, intermediate and final phases is represented in Figure 30. The available time resolution was insufficient to capture the initial formation of the intermediate species, and the low signal-to-noise ratio of the *in-situ* data likely explains why the refined wt% values of the intermediates do not fall to zero.

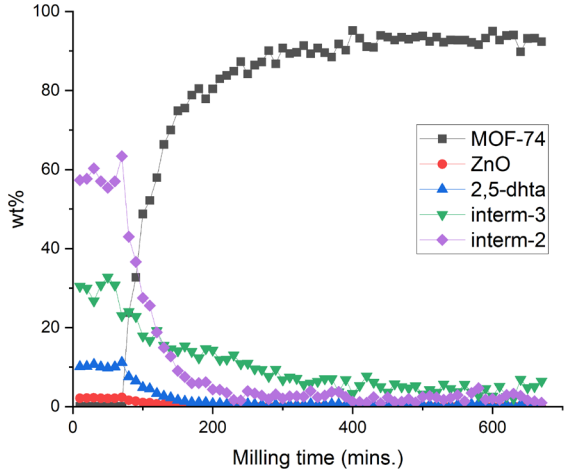

Figure 30. Quantitative analysis, obtained from Rietveld multiphase refinement, for the *in-situ* reaction showing the consumption of ZnO and 2,5-dihydroxyterephthalic acid starting reactants, while the target product MOF-74 is formed. Intermediate phases 2 and 3 according to Beamish-Cook *et al*.[7]

The powder obtained from the milling synthesis was measured in an 8 mm vanadium can on GEM, and the corresponding Rietveld refinement (see result in Figure 31) indicates that the formation of the target MOF-74 phase was complete. However, the *in-situ* data collected during milling exhibited notably low intensity. This is most likely due to a substantial fraction of the sample lying outside the neutron beam footprint, as the reactor diameter is considerably larger than the maximum beam width. Consequently, only a limited portion of the powder was effectively illuminated, reducing the observable diffraction signal.

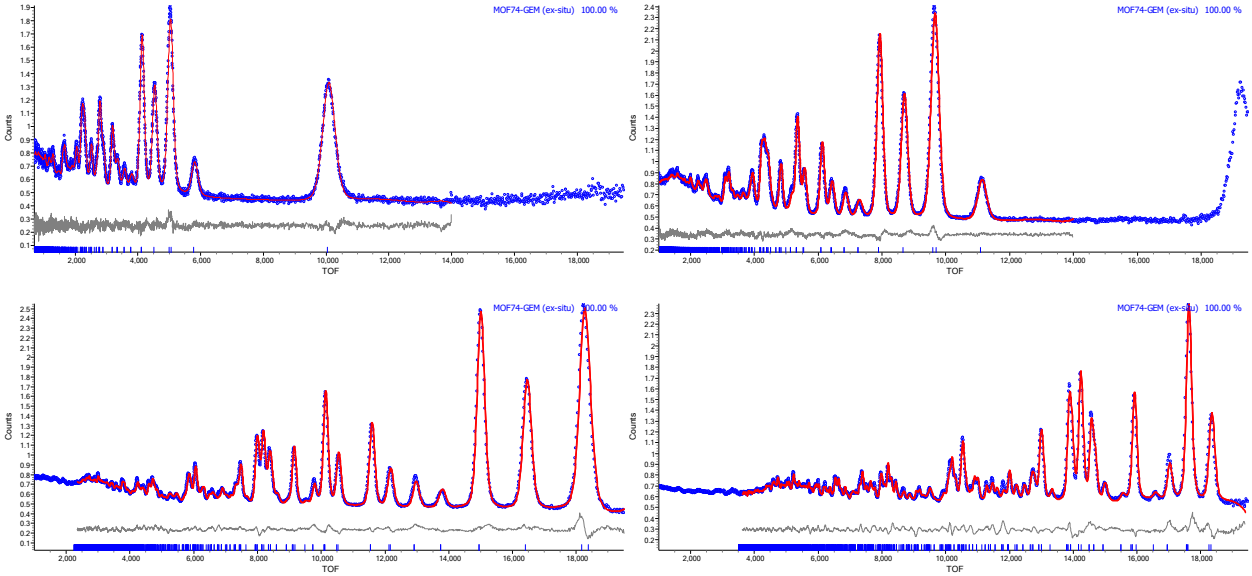

Figure 31. Rietveld refinement result plots for detector banks #1 to #4 (left to right and top to bottom), using data collected form the synthesized MOF-74 material, which was loaded into an 8mm diameter vanadium sample holder.

Synthesis reaction	Reactor / balls material
Copper acetate monohydrate + 1,3,5-benzenetricarboxylic acid (BTC) → HKUST-1 metal-organic-framework; LAG (liquid assisted grinding) with D_2O	Aluminium (spherical reactor)

Figure 32 shows the GEM *in-situ* data from the HKUST-1 synthesis reaction as a function of time, using a spherical aluminium reactor and balls. Apart from the very intense aluminium diffraction peaks, some low-intensity diffraction peaks from the starting and target compounds are observable.

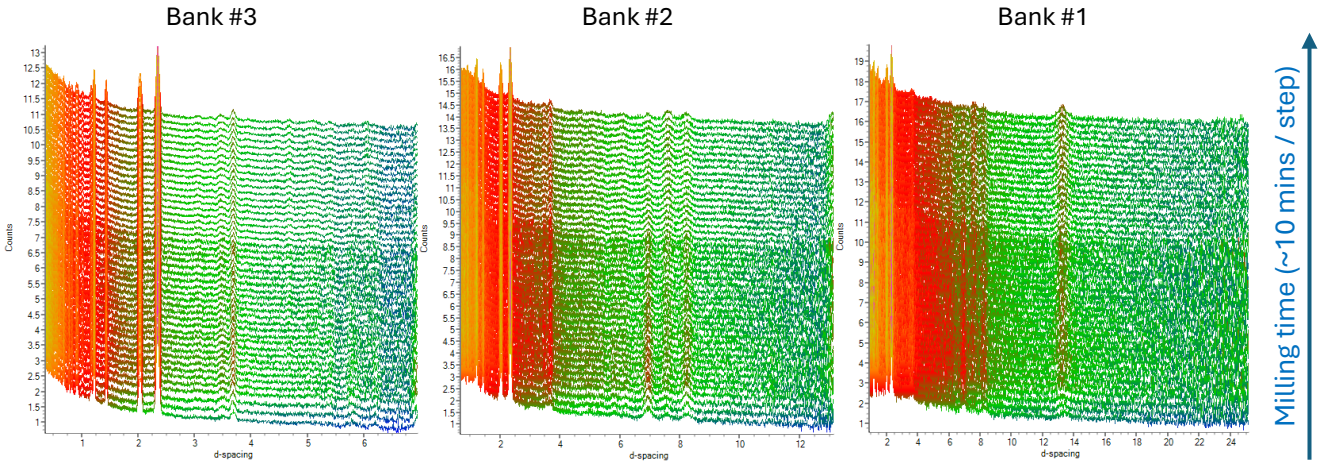

Figure 32. *In-situ* diffraction data, collected during mechanosynthesis of HKUST-1 material, for selected GEM detector banks. An offset has been applied along Y axis for better visualisation.

A rapid transformation of the starting reactants is observed during the first few minutes of ball milling. Beyond this initial stage, however, the reaction appears to stall, with no further meaningful evolution in the diffraction patterns. The *in-situ* measurements indicate that the formation of the target HKUST-1 phase remains incomplete: although some product is generated, a substantial portion of the starting materials persists. This is corroborated by the Rietveld refinement of the *ex-situ* X-ray diffraction data collected from the final powder (Figure 33), which confirms only partial conversion with a yield of about 31%.

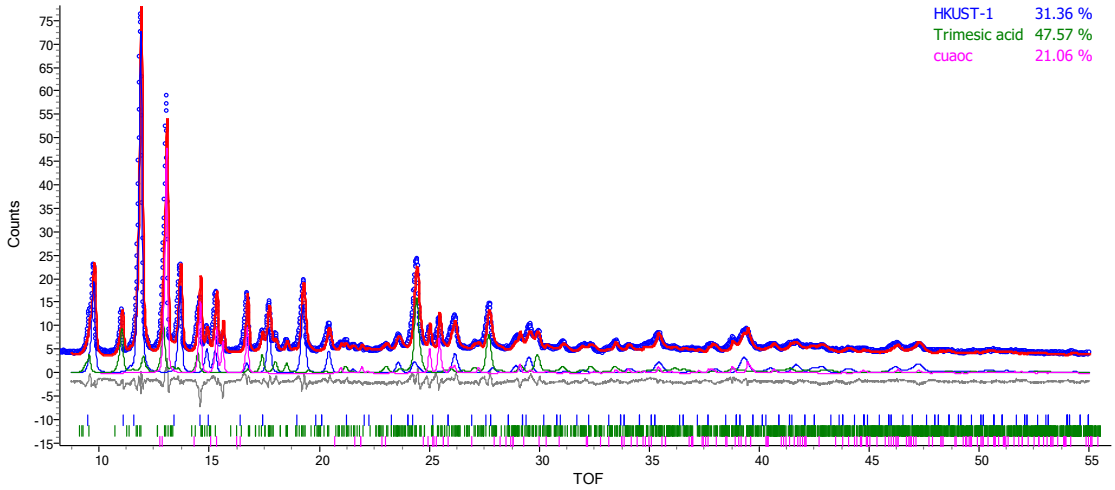

Figure 33. Rietveld refinement plot for the synthesised HKUST-1 powder material, measured on a D2 Phaser X-ray diffractometer.

Synthesis reaction	Reactor / balls material
ZnO + 2,5-dihydroxyterephthalic acid → MOF-74 metal-organic-framework; LAG (liquid assisted grinding) with DMF	PTFE (cylindrical reactor + stainless-steel balls)

Figure 34 shows the GEM *in-situ* data from the MOF-74 synthesis reaction as a function of time, using a PTFE reactor and stainless-steel balls. Apart from the very intense PTFE and stainless-steel diffraction peaks, some low-intensity diffraction peaks from the starting and target compounds are observable.

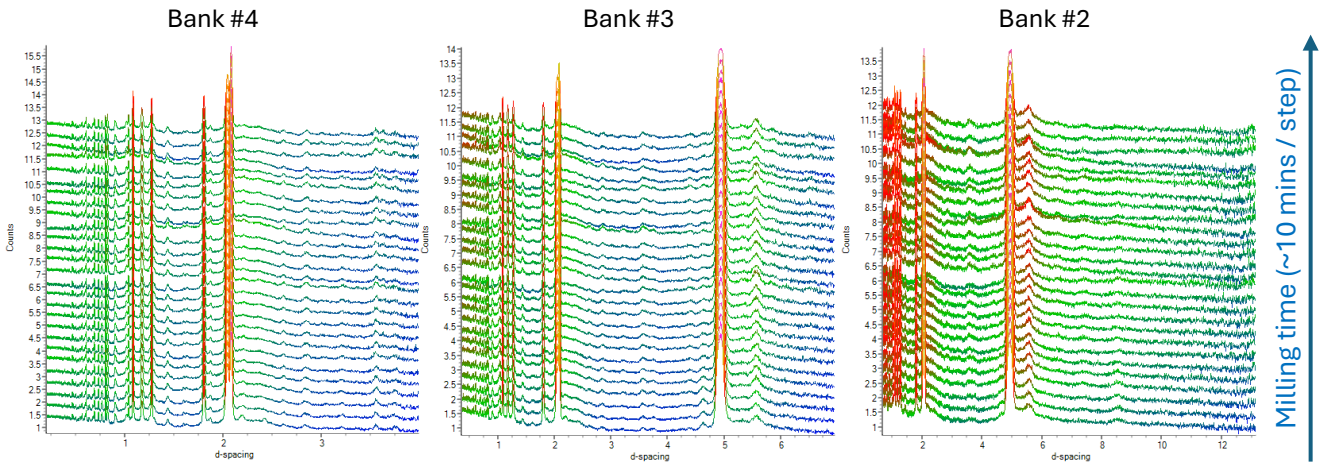

Figure 34. *In-situ* diffraction data, collected during mechanosynthesis of MOF-74 material, for selected GEM detector banks. An offset has been applied along Y axis for better visualisation.

A very subtle difference between the first and last diffraction patterns can be discerned, but no clear transformation of the starting reactants is evident. Figure 35 shows the Rietveld refinement of the final powder product, measured on a D2 Phaser X-ray diffractometer. The refinement confirms that the synthesis reaction did initiate, yielding approximately 22 wt% of the target MOF-74 phase (highlighted in blue). However, a substantial proportion of the initial reactants remains unconverted. A positive outcome is that the intermediate phase is clearly identifiable in the X-ray data, even though it is difficult to detect in the neutron diffraction measurements.

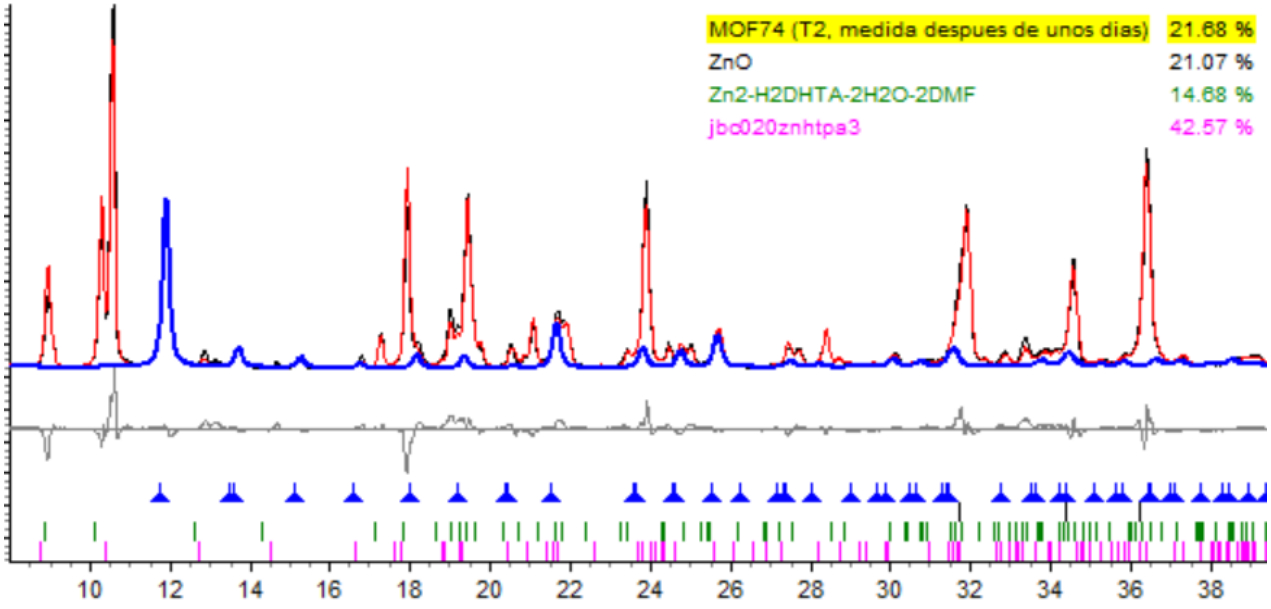

Figure 35. Rietveld refinement plot for the synthesised MOF-74 powder material (its diffraction contribution highlighted in blue), measured on a D2 Phaser X-ray diffractometer.

Synthesis reaction	Reactor / balls material
$RbCl + CuBr_2 \rightarrow Rb_2CuCl_2Br_2$; LAG (liquid assisted grinding) with DMF	PTFE (cylindrical reactor)

Figure 36 shows the GEM *in-situ* data from the $Rb_2CuCl_2Br_2$ synthesis reaction as a function of time, using a PTFE reactor and balls. Apart from the very intense PTFE diffraction peak, some low-intensity diffraction peaks from the starting and target compounds are observable.

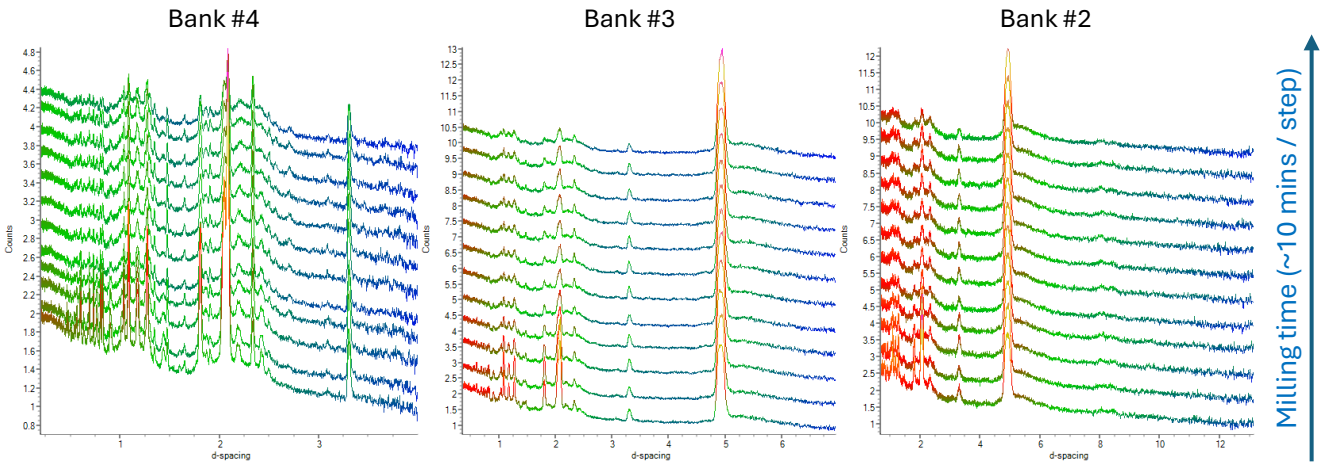

Figure 36. *In-situ* diffraction data, collected during mechanosynthesis of $Rb_2CuCl_2Br_2$ material, for selected GEM detector banks. An offset has been applied along Y axis for better visualisation.

Only a very slight evolution is visible, primarily on detector bank #4, and no substantial progression of the reaction can be identified. This suggests that the PTFE milling balls do not provide sufficient energy to the powder to effectively initiate the mechanochemical process. The diffraction pattern of the final powder, measured on a Miniflex X-ray diffractometer (Figure 37), confirms that the reaction did not reach completion: the diffraction pattern still shows strong contributions from the starting reactants, along with additional intensity from one or more unidentified phases. Overall, the milling energy delivered by the PTFE balls appears inadequate, a limitation that becomes even more pronounced when working with the larger sample quantities required for *in-situ* neutron experiments.

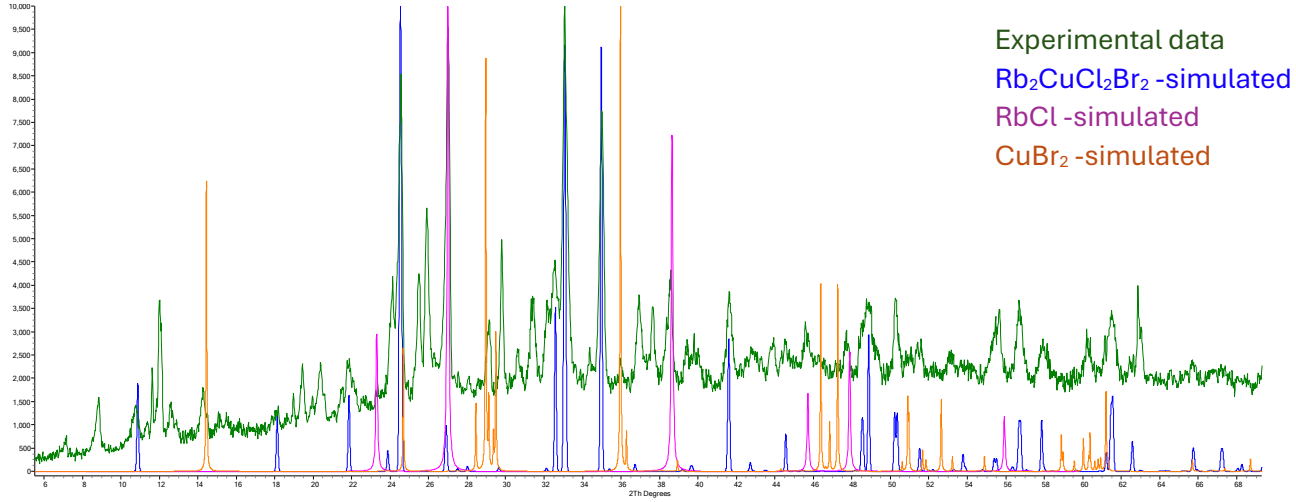

Figure 37. Comparison of the experimental data for the resulting powder material, measured on a D2 Phaser X-ray diffractometer, with the theoretical pattern for the target compound $Rb_2CuCl_2Br_2$, and the initial reactants RbCl and $CuBr_2$.

Synthesis reaction	Reactor / balls material
ZnO + 2-methylimidazole (mim) → ZIF-8 metal-organic-framework; LAG (liquid assisted grinding) with DMF	Aluminium (cylindrical reactor) + stainless-steel balls

Figure 38 shows the GEM *in-situ* data from the ZIF-8 synthesis reaction as a function of time, using a cylindrical aluminium reactor and stainless-steel balls. Apart from the very intense aluminium and stainless-steel diffraction peak, some low-intensity diffraction peaks from the starting and target compounds are observable.

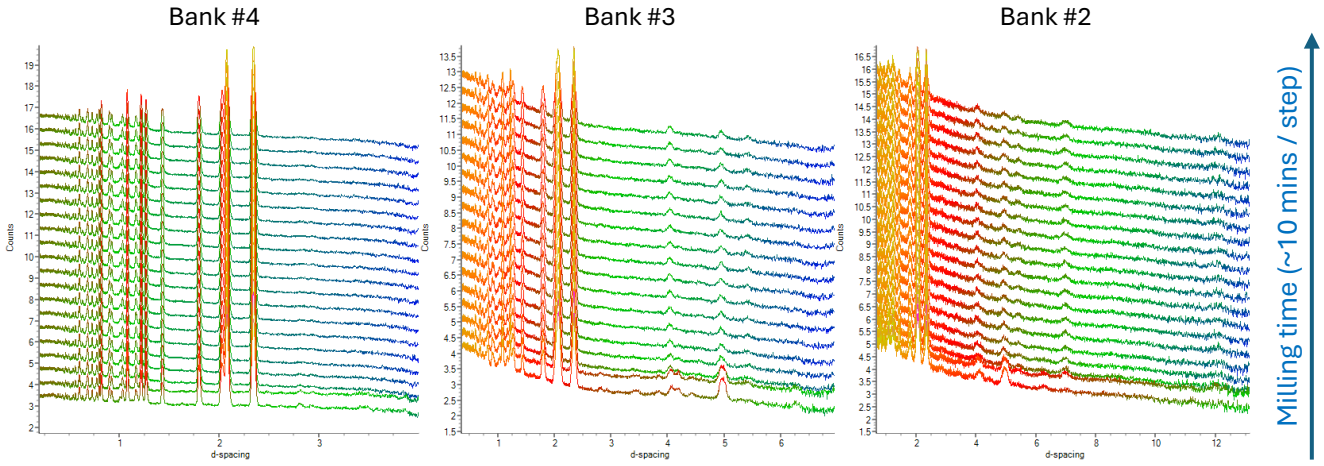

Figure 38. *In-situ* diffraction data, collected during mechanosynthesis of ZIF-8 material, for selected GEM detector banks. An offset has been applied along Y axis for better visualisation.

A rapid reaction is observed during the initial stages of the *in-situ* measurements, but the transformation appears to halt after roughly 30 minutes. Figure 39 presents the Rietveld refinement corresponding to the reaction onset (first-step diffraction data). Notably, even before the ball-milling process begins, a measurable amount of the target ZIF-8 phase is already present in the reactor. This indicates that the reactants can partially form ZIF-8 under LAG conditions without receiving mechanical energy from the milling balls.

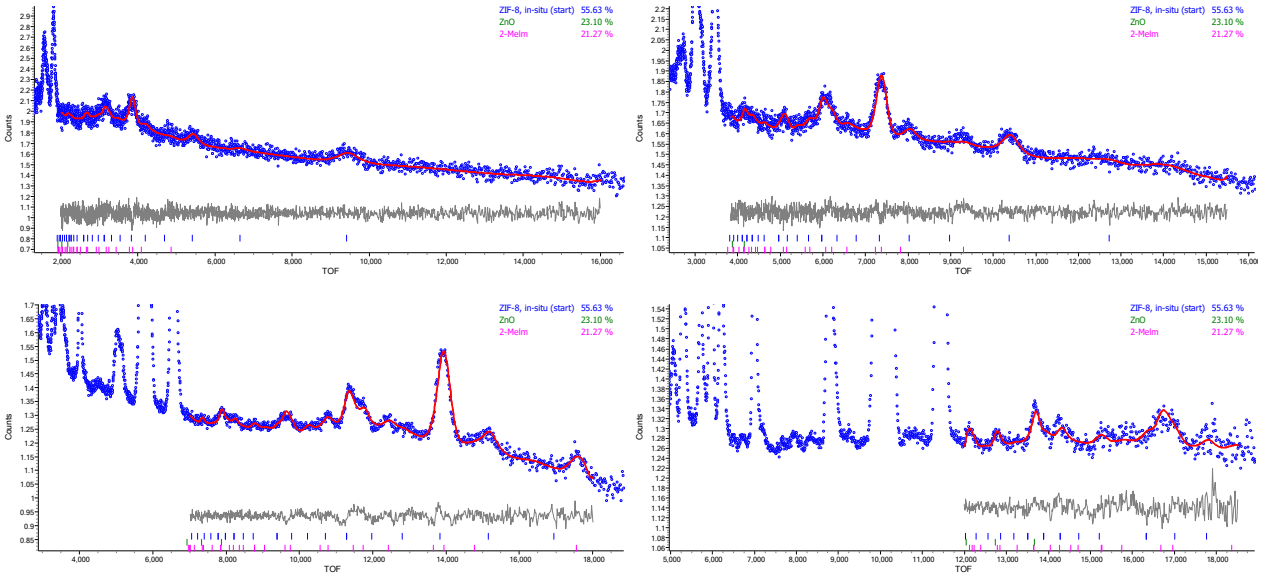

Figure 39. Rietveld refinement result plots for detector banks #1 to #4 (left to right and top to bottom), using the first collected dataset during *in-situ* mechanosynthesis of ZIF-8 material.

Rietveld refinement of the final-step diffraction data shows that, for this reaction test, full conversion was achieved: a 100 wt% pure ZIF-8 phase was successfully refined from the *in-situ* dataset (see Figure 40). Achieving complete reaction required the use of stainless-steel milling balls, which provide sufficient impact energy for the mechanochemical transformation to proceed to completion.

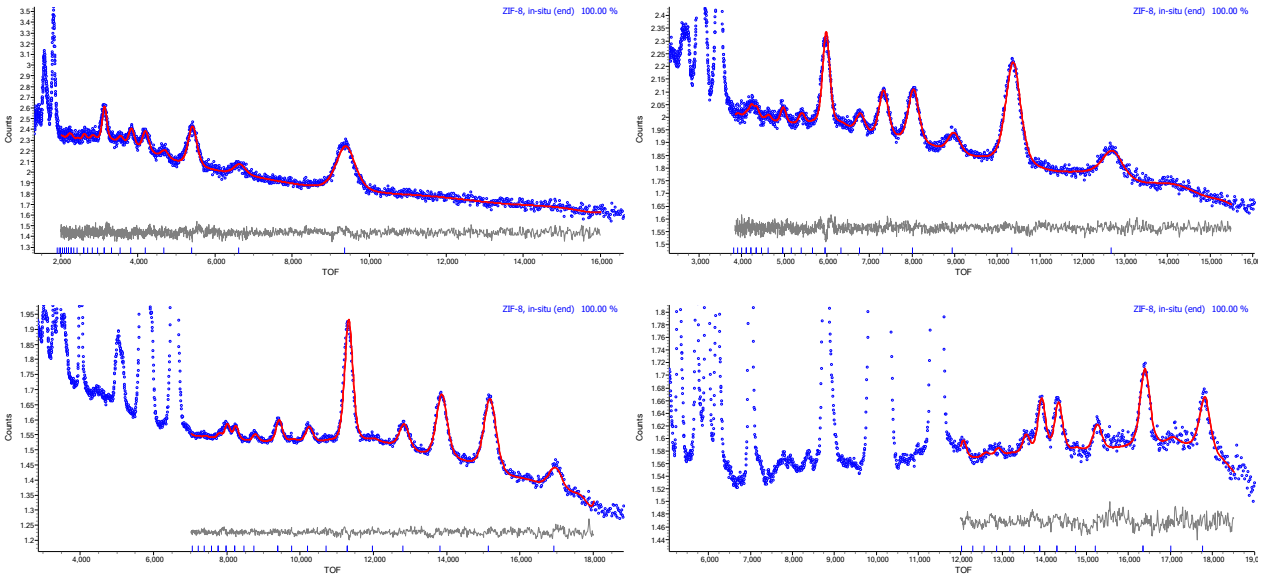

Figure 40. Rietveld refinement result plots for detector banks #1 to #4 (left to right and top to bottom), using the last collected dataset during *in-situ* mechanosynthesis of ZIF-8 material.

The powder obtained from the milling synthesis was loaded into an 8 mm vanadium can and measured on GEM. The Rietveld refinement shown in Figure 41 demonstrates that a good fit can be achieved for the target ZIF-8 crystalline phase, indicating that the *in-situ* data were of comparable quality to the *ex-situ* measurement—apart from the additional diffraction peaks arising from the aluminium components of the reactor.

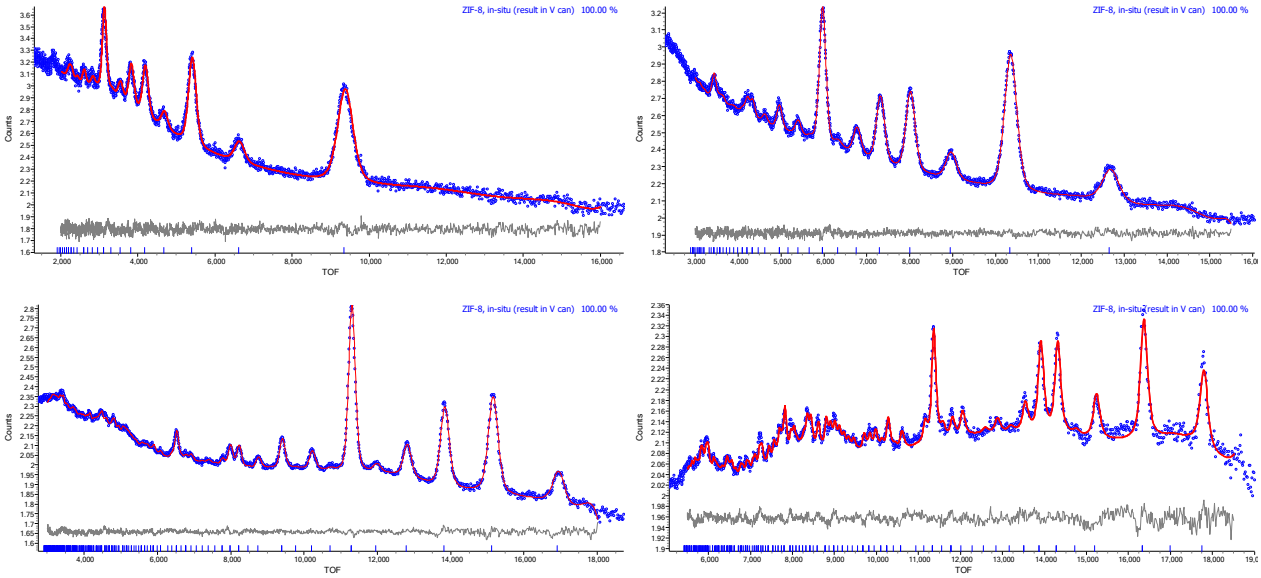

Figure 41. Rietveld refinement result plots for detector banks #1 to #4 (left to right and top to bottom), using data collected form the synthesized ZIF-8 material, which was loaded into an 8mm diameter vanadium sample holder.

Synthesis reaction	Reactor / balls material
$CsCO_3 + MoO_3 \rightarrow Cs_6[Mo_7O_{24}]$; LAG (liquid assisted grinding) with D_2O	Aluminium (cylindrical reactor) + steel balls

Figure 42 shows the GEM *in-situ* data from the $Cs_6[Mo_7O_{24}]$ synthesis reaction as a function of time, using a cylindrical aluminium reactor and stainless-steel balls. Apart from the very intense aluminium and stainless-steel diffraction peak, some very low-intensity diffraction peaks are observable.

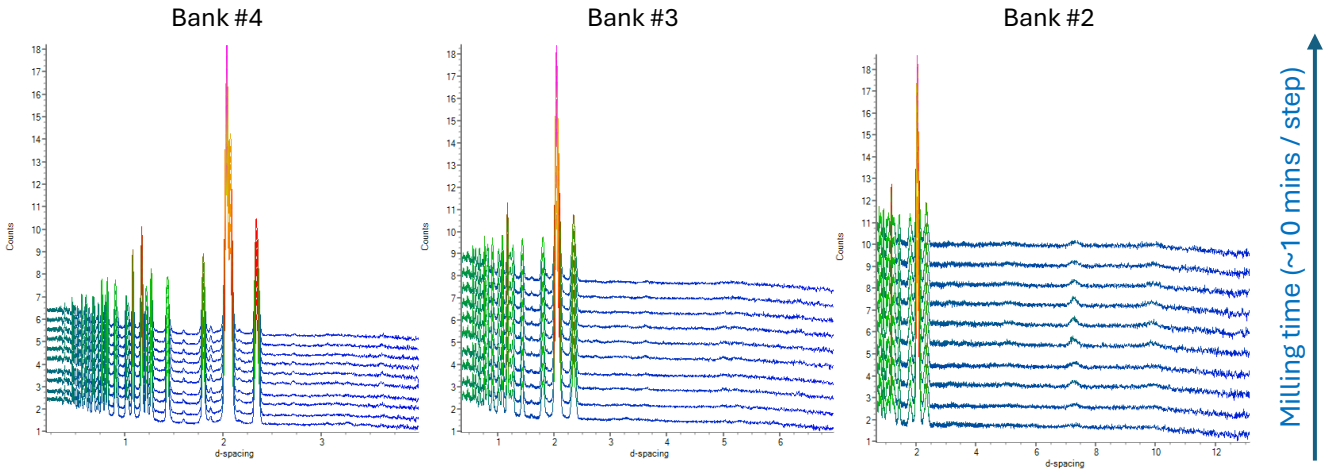

Figure 42. *In-situ* diffraction data, collected during mechanosynthesis of $Cs_6[Mo_7O_{24}]$ material, for selected GEM detector banks. An offset has been applied along Y axis for better visualisation.

For this reaction test, a slight evolution appears to occur, but the diffraction intensity from the powder inside the reactor is extremely low—most likely due to the small volume of reactants used. The powder obtained from the milling synthesis was subsequently loaded into a 6 mm vanadium can and measured on GEM. The Rietveld refinement shown in Figure 43 demonstrates that a good fit can be achieved for the target $Cs_6[Mo_7O_{24}]$ crystalline phase, indicating that the reaction did (in principle) proceed during the *in-situ* experiment, even though the transformation could not be directly detected from the low-intensity *in-situ* data.

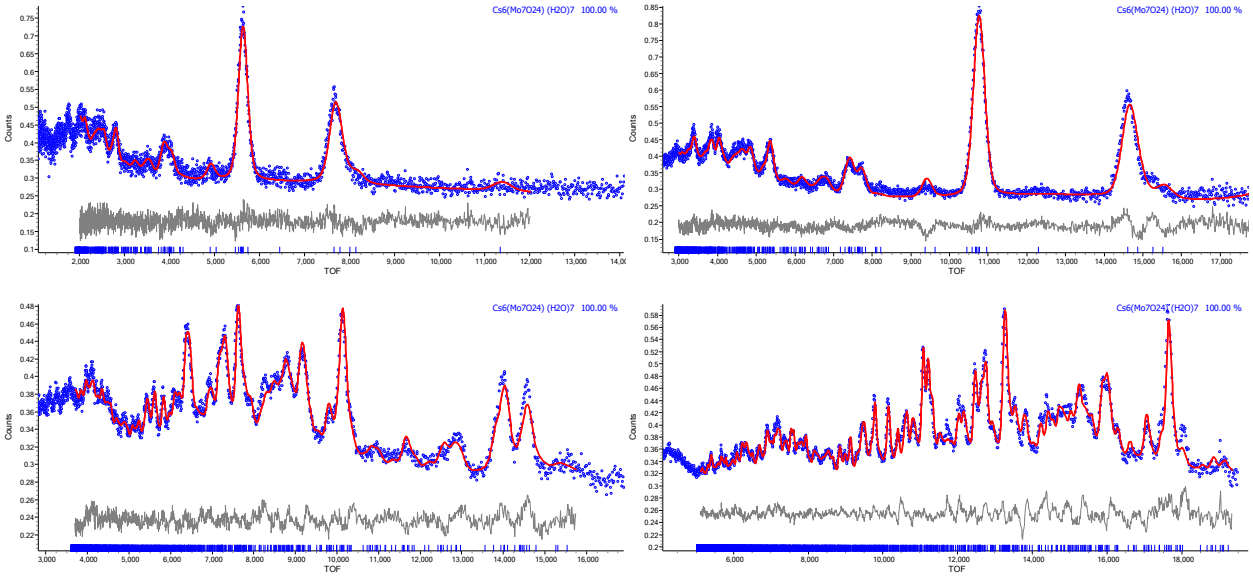

Figure 43. Rietveld refinement result plots for detector banks #1 to #4 (left to right and top to bottom), using data collected form the synthesized $Cs_6[Mo_7O_{24}]$ material, which was loaded into a 6mm diameter vanadium sample holder.

Synthesis reaction	Reactor / balls material
$CsCO_3 + MoO_3 \rightarrow Cs_6[Mo_7O_{24}]$; LAG (liquid assisted grinding) with D_2O	10 mm diameter vanadium reactor (cylindrical) and vanadium balls

Figure 44 shows the GEM *in-situ* data from the $Cs_6[Mo_7O_{24}]$ synthesis reaction as a function of time, using a 10mm diameter cylindrical vanadium reactor and balls. A 60 mm spacer was added in between the ball-mill and the GEM Tomkinson flange for correct beam-to-sample adjustment. Only diffraction peaks from the starting and final materials are observable.

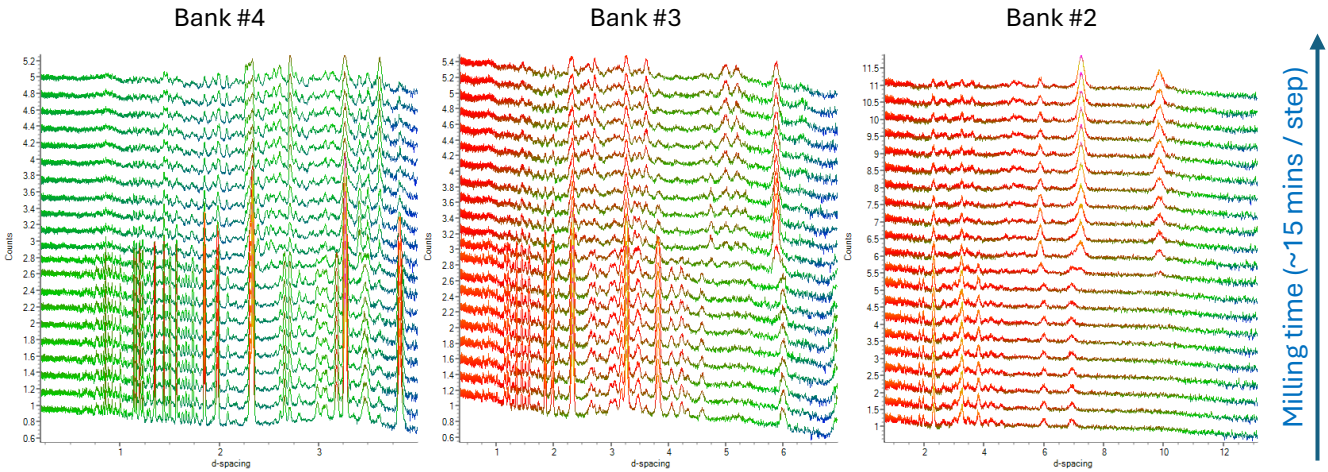

Figure 44. *In-situ* diffraction data, collected during mechanosynthesis of $Cs_6[Mo_7O_{24}]$ material, for selected GEM detector banks. An offset has been applied along Y axis for better visualisation.

The *in-situ* diffraction data clearly capture the evolution of the materials throughout the mechanochemical reaction, finishing in the formation of the final product. To prevent premature reaction, the starting powders must be loaded into the reactor in the specific order $CsCO_3$ (bottom), MoO_3 (top), and finally D_2O (on top); otherwise, the reaction appears to initiate even without milling. Figure 45 shows the Rietveld refinement of the first-step diffraction data, collected before milling begins, where only diffraction contributions from the starting materials are observed.

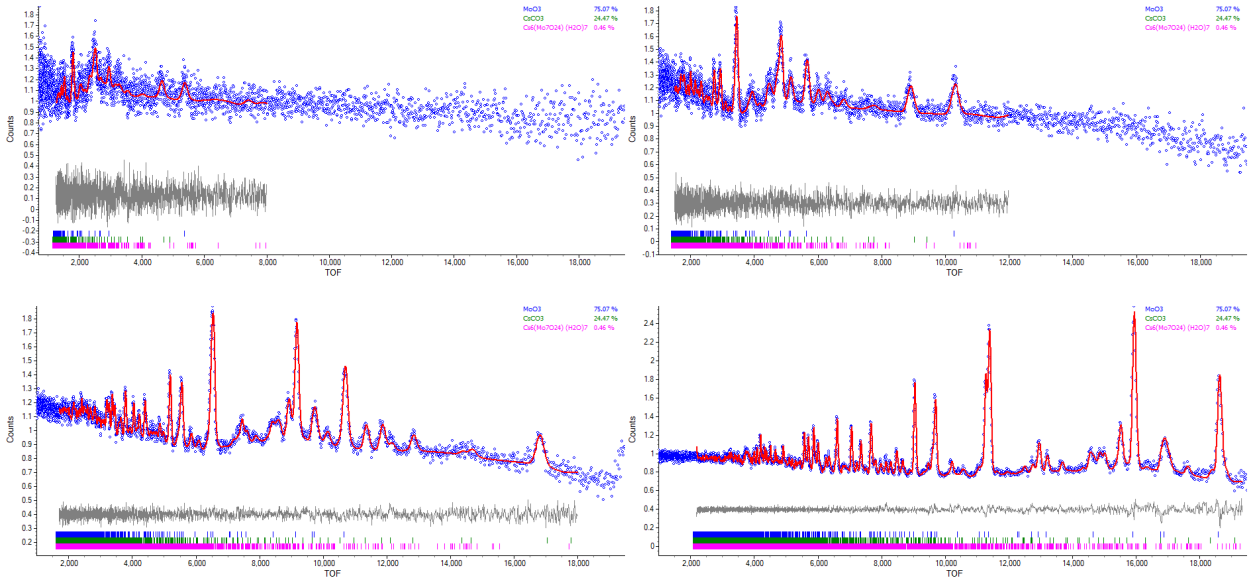

Figure 45. Rietveld refinement result plots for detector banks #1 to #4 (left to right and top to bottom), using the first collected dataset during *in-situ* mechanosynthesis of $Cs_6[Mo_7O_{24}]$ material.

Figure 46 shows the Rietveld refinement of the final-step diffraction data, collected at the end of the milling process. The diffraction contributions from both reactants have completely disappeared, and only the reflections of the target compound remain, confirming that the reaction proceeded to full completion as expected.

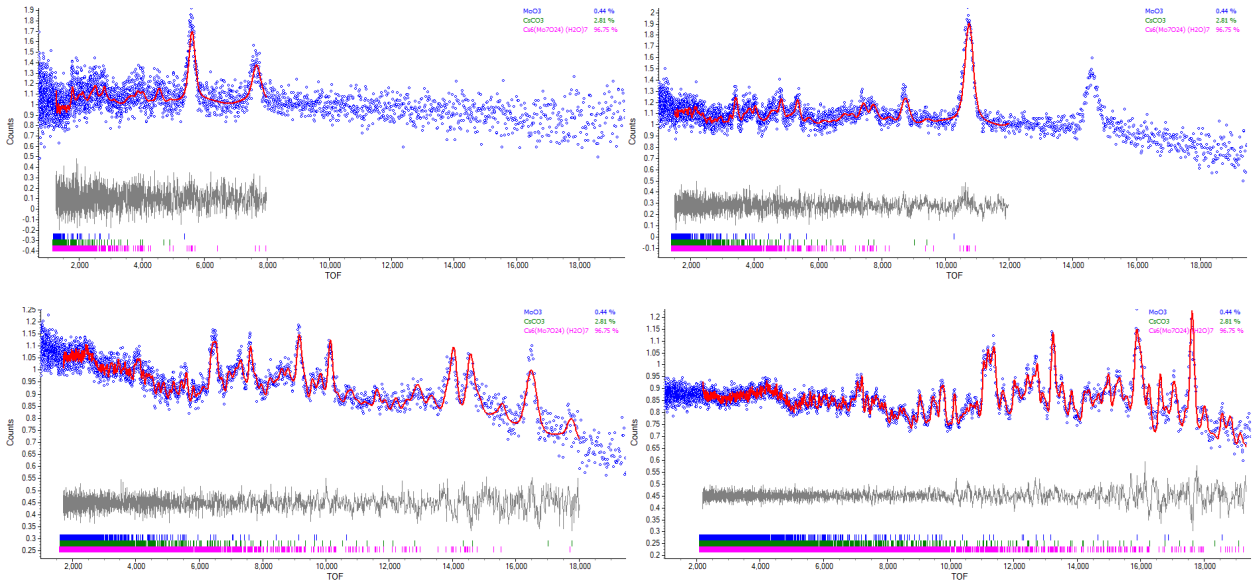

Figure 46. Rietveld refinement result plots for detector banks #1 to #4 (left to right and top to bottom), using the last collected dataset during *in-situ* mechanosynthesis of $Cs_6[Mo_7O_{24}]$ material.

A sequential Rietveld refinement was performed across all measurement steps, and the resulting wt% evolution of the starting and final phases is shown in Figure 47. The final $Cs_6[Mo_7O_{24}]$ compound was almost completely obtained, and the refinement reveals a direct conversion of the starting materials into the final product, with no evidence of any intermediate phase forming during the reaction. Note that this graph does not show a smooth reaction, as the poor signal-to-noise ratio on the diffraction data doesn't allow for a precise quantitative refinement.

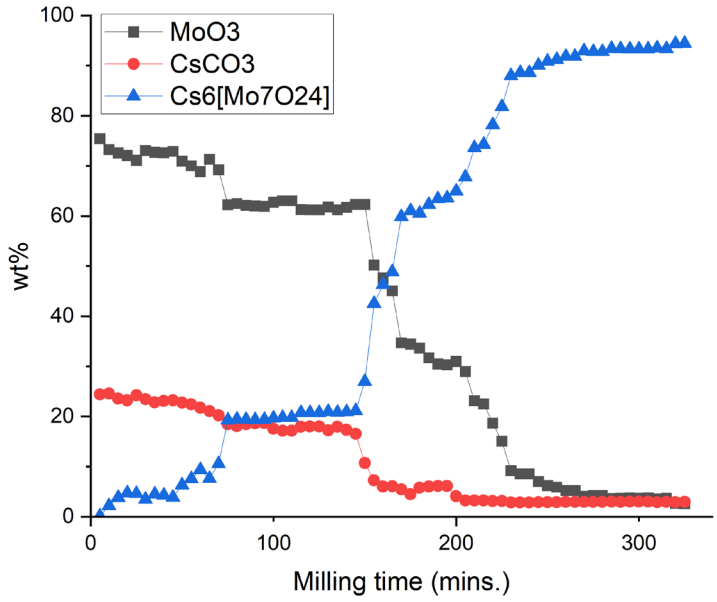

Figure 47. Quantitative analysis, obtained from Rietveld multiphase refinement, for the *in-situ* reaction showing the consumption of MoO_3 and $CsCO_3$ starting reactants, while the target product $Cs_6[Mo_7O_{24}]$ is formed.

Synthesis reaction	Reactor / balls material
Pyrazinamide ($C_5H_5N_3O$) + Oxalic acid ($C_2H_2O_4$) →Pyra-Oxal co-crystal	15 mm diameter vanadium reactor (cylindrical) and vanadium balls

Figure 48 shows the GEM *in-situ* data from the Pyra-Oxal co-crystal synthesis reaction as a function of time, using a 15mm diameter cylindrical vanadium reactor and balls. A 60 mm spacer was added in between the ball-mill and the GEM Tomkinson flange for correct beam-to-sample adjustment. Only diffraction peaks from the starting and final materials are observable.

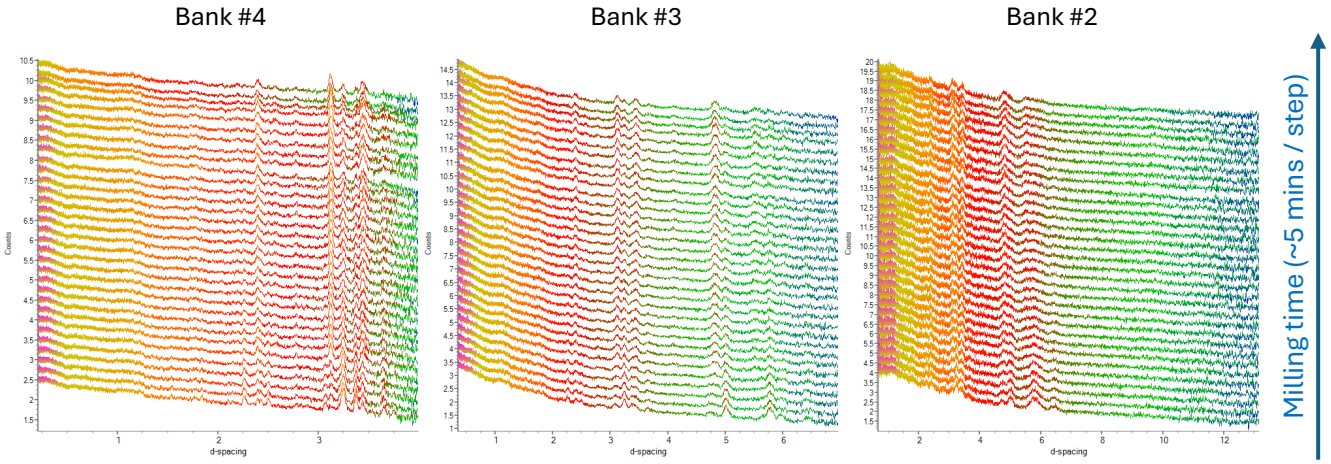

Figure 48. *In-situ* diffraction data, collected during mechanosynthesis of Pyra-Oxal co-crystal material, for selected GEM detector banks. An offset has been applied along Y axis for better visualisation.

This reaction test was carried out using a larger 15 mm-diameter vanadium can fitted with a newly adapted lid. Although the diffraction peak intensities are relatively low, the data indicate that a reaction did occur; however, despite progressing substantially, it appears not to have reached full completion. Figure 49 shows the Rietveld refinement of the first-step diffraction data, collected before milling begins, where only the diffraction contributions from the starting materials are present. The small refined wt% of the final target phase is probably not real and most likely a consequence of the low signal-to-noise ratio.

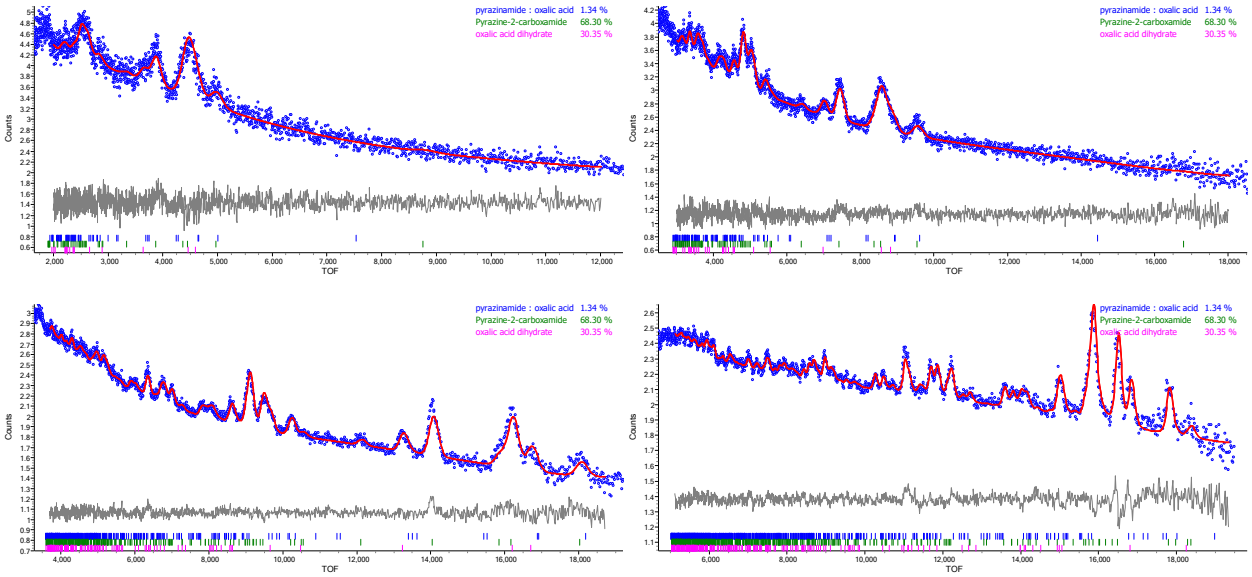

Figure 49. Rietveld refinement result plots for detector banks #1 to #4 (left to right and top to bottom), using the first collected dataset during *in-situ* mechanosynthesis of Pyra-Oxal co-crystal material.

Figure 50 shows the Rietveld refinement of the final-step diffraction data, collected at the end of the milling process. Diffraction contributions from both the target phase and the starting materials are still present, indicating that the reaction did not proceed to full completion, as the estimated wt% of the target compound is around 73%.

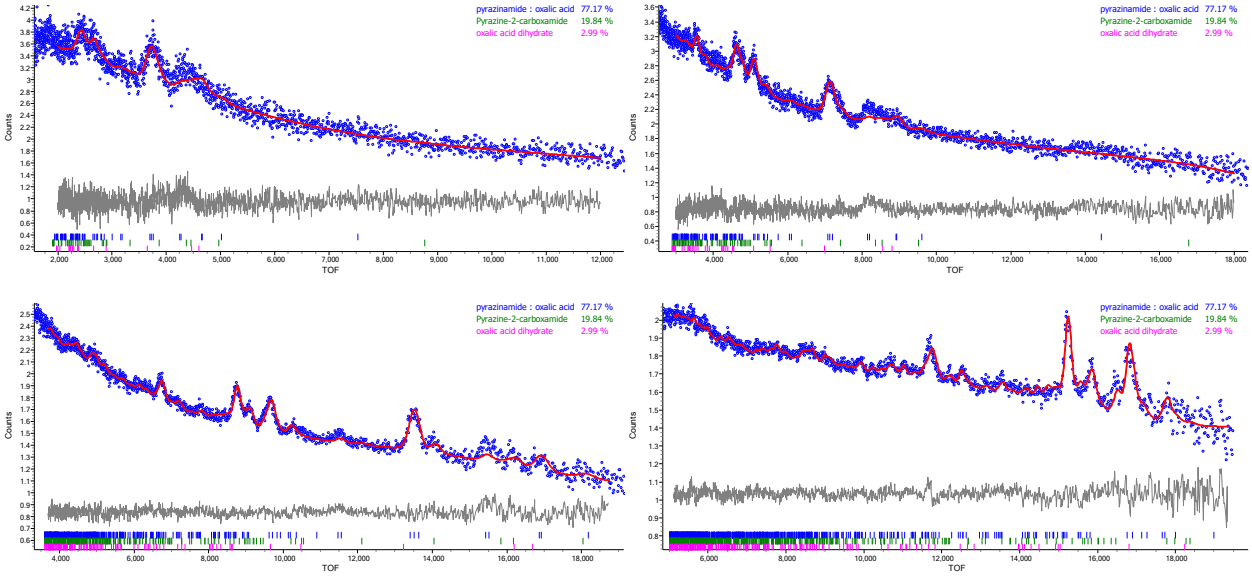

Figure 50. Rietveld refinement result plots for detector banks #1 to #4 (left to right and top to bottom), using the last collected dataset during *in-situ* mechanosynthesis of Pyra-Oxal co-crystal material.

A sequential Rietveld refinement was performed across all measurement steps, and the resulting wt% evolution of the starting and final phases is shown in Figure 51. Although the final Pyra–Oxal co-crystal was not fully obtained, the refinement reveals a direct conversion of the starting materials into the final product, with no evidence of any intermediate phase forming during the reaction.

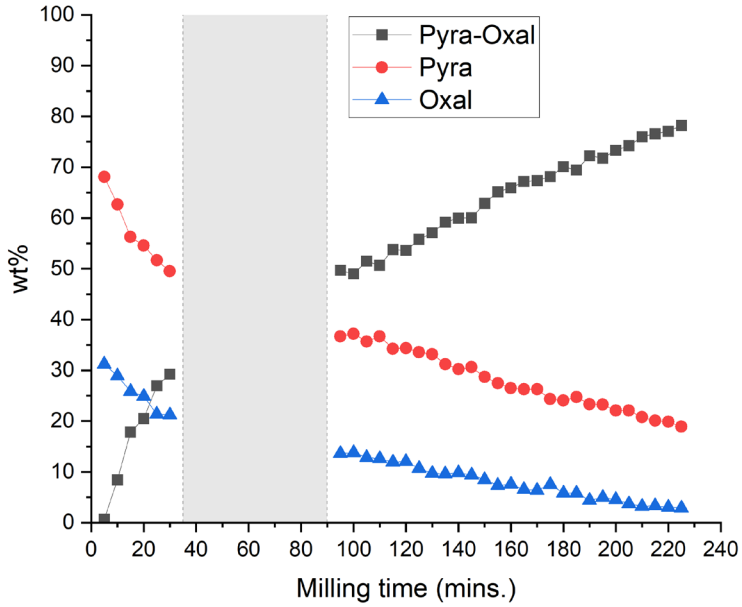

Figure 51. Quantitative analysis, obtained from Rietveld multiphase refinement, for the *in-situ* reaction showing the consumption of Pyrazinamide and Oxalic Acid starting reactants, while the target product Pyra-Oxal co-crystal is formed. The shadowed region corresponds to a time window when the neutron beam was lost and no diffraction data could be collected.

The powder obtained from the milling synthesis was loaded into an 8 mm vanadium can and measured on GEM, and Figure 52 shows the corresponding Rietveld refinement. A noticeably improved signal-to-noise ratio is observed, as the same sample volume is now more effectively packed within the smaller container. A satisfactory multiphase refinement could be achieved, confirming that the reaction did occur during the *in-situ* test, although it did not reach completion. As expected, the diffraction signal is slightly better than in the *in-situ* data, where the sample was less densely packed. Moreover, the refined wt% of the target phase has increased to approximately 88 %, suggesting that the reaction may have continued to progress after the *in-situ* experiment ended.

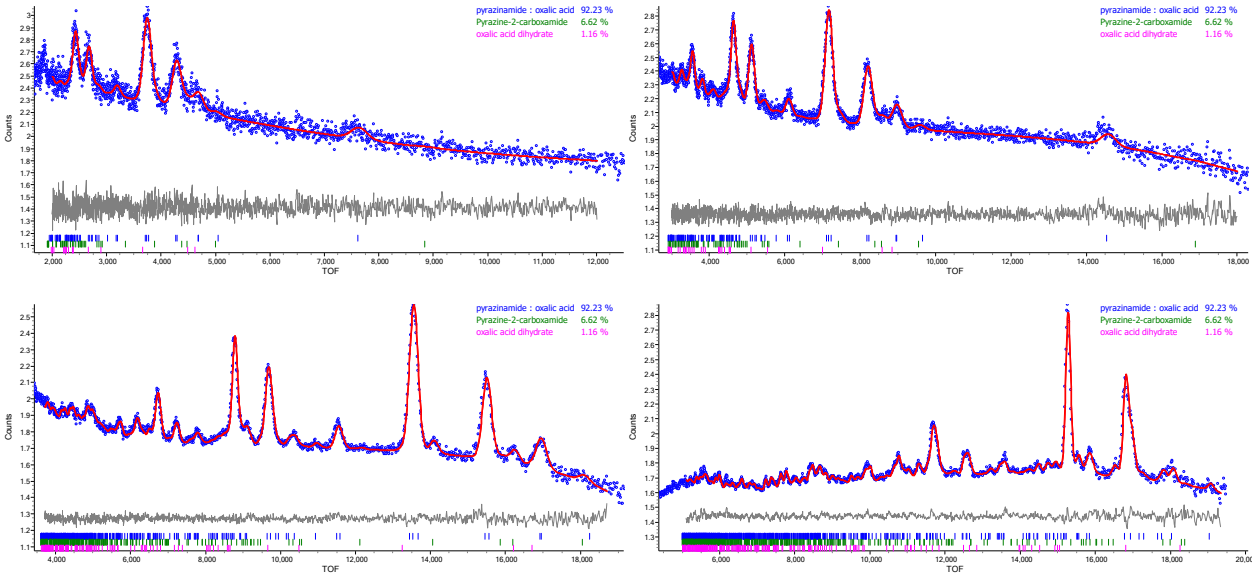

Figure 52. Rietveld refinement result plots for detector banks #1 to #4 (left to right and top to bottom), using data collected form the synthesized Pyra-Oxal co-crystal material, which was loaded into an 8mm diameter vanadium sample holder.

Synthesis reaction	Reactor / balls material
ZnO + 2-methylimidazole (mim) → ZIF-8 metal-organic-framework; LAG (liquid assisted grinding) with DMF	10 mm diameter vanadium reactor (cylindrical) and vanadium balls

Figure 53 shows the GEM *in-situ* data from the ZIF-8 synthesis reaction as a function of time, using a 10mm diameter cylindrical vanadium reactor and balls. A 60 mm spacer was added in between the ball-mill and the GEM Tomkinson flange for correct beam-to-sample adjustment, and deuterated 2-methylimidazole reactant was used in this test. Only diffraction peaks from the starting and final materials are observable.

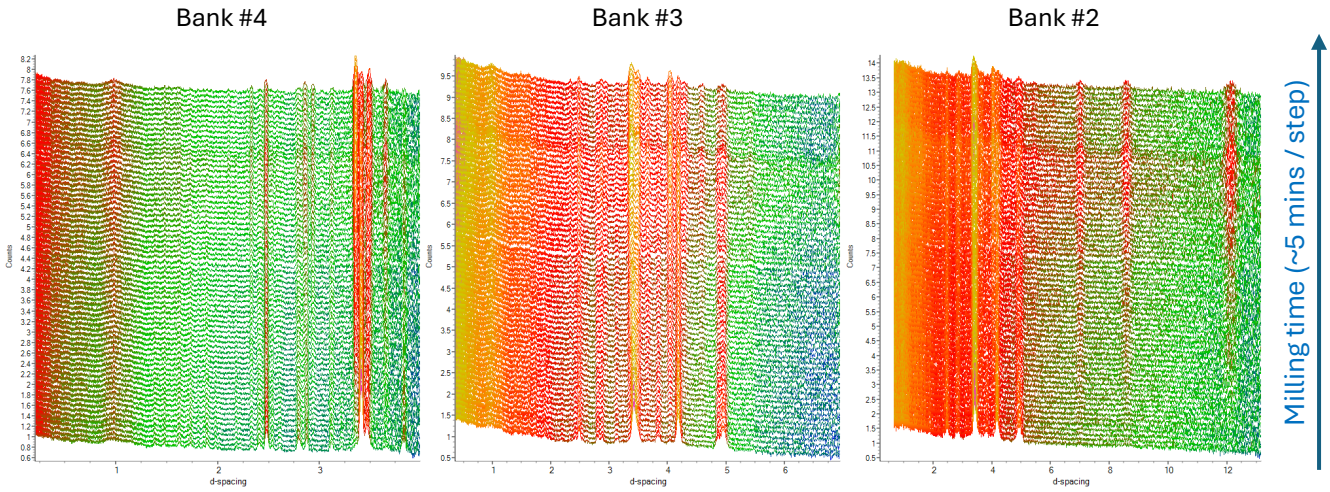

Figure 53. *In-situ* diffraction data, collected during mechanosynthesis of ZIF-8 material, for selected GEM detector banks. An offset has been applied along Y axis for better visualisation.

The use of deuterated 2-methylimidazole significantly improved the diffraction quality, avoiding the elevated background typically introduced by hydrogen. Although the overall peak intensities remain relatively low, the data nonetheless confirm that a reaction took place. However, despite substantial progress, the reaction did not reach full completion, as diffraction contributions from the starting materials are still visible in the final dataset. Figure 54 presents the Rietveld refinement of the first-step diffraction data, collected after 5 minutes of milling, where initial diffraction from the target phase is already detectable. This indicates that the reaction initiates rapidly, although the refined wt% of the product at this early stage is likely overestimated, most probably due to the low signal-to-noise ratio.

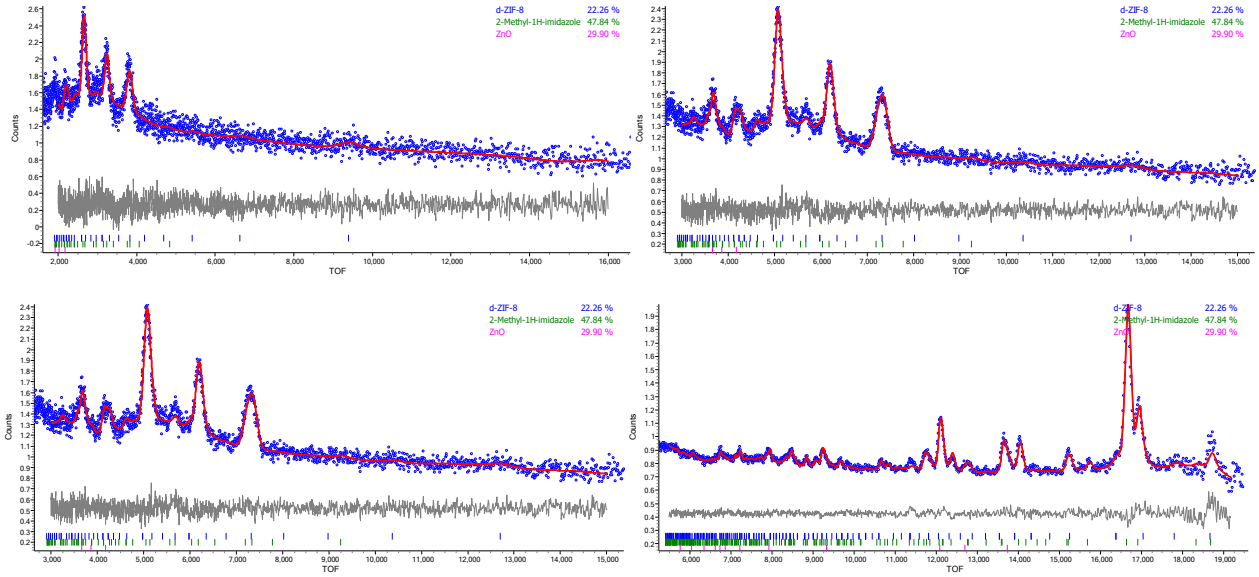

Figure 54. Rietveld refinement result plots for detector banks #1 to #4 (left to right and top to bottom), using the first collected dataset during *in-situ* mechanosynthesis of ZIF-8 material.

Figure 55 shows the Rietveld refinement of the final-step diffraction data, collected at the end of the milling process. Diffraction contributions from both the target phase and the starting materials remain visible, confirming that the reaction did not reach full completion. The refined wt% of the target compound is approximately 85%, consistent with the presence of residual reactants in the final dataset.

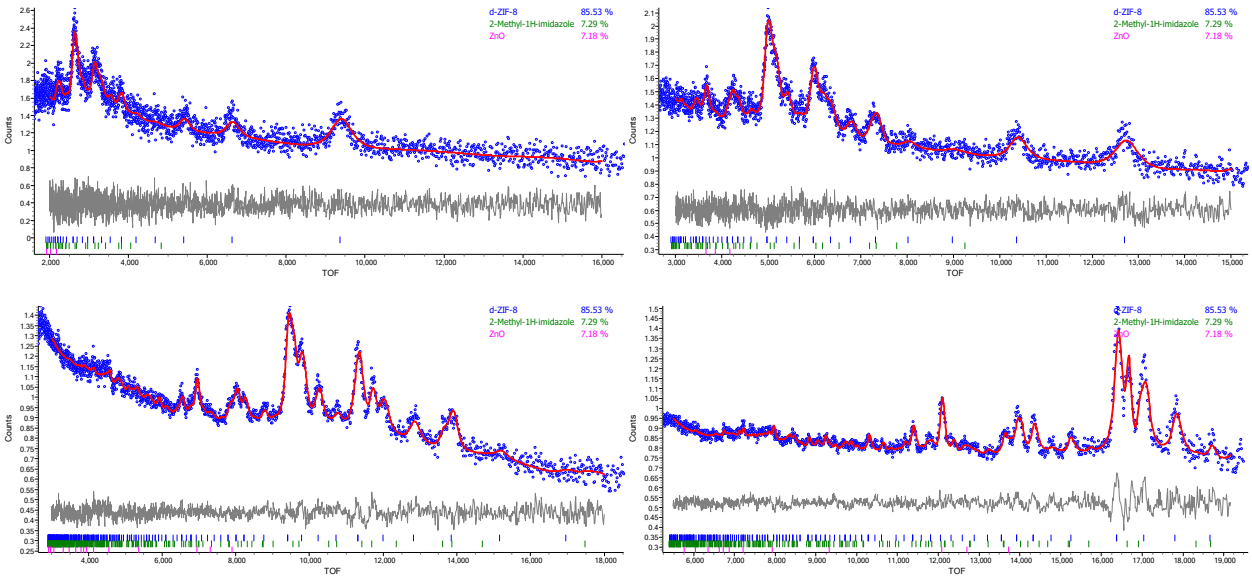

Figure 55. Rietveld refinement result plots for detector banks #1 to #4 (left to right and top to bottom), using the last collected dataset during *in-situ* mechanosynthesis of ZIF-8 material.

A sequential Rietveld refinement was performed across all measurement steps, and the resulting wt% evolution of the starting and final phases is shown in Figure 56. Although the final ZIF-8 product was not fully obtained, the refinement indicates a direct conversion of the starting materials into the final phase, with no evidence of any intermediate species forming at any point during the reaction.

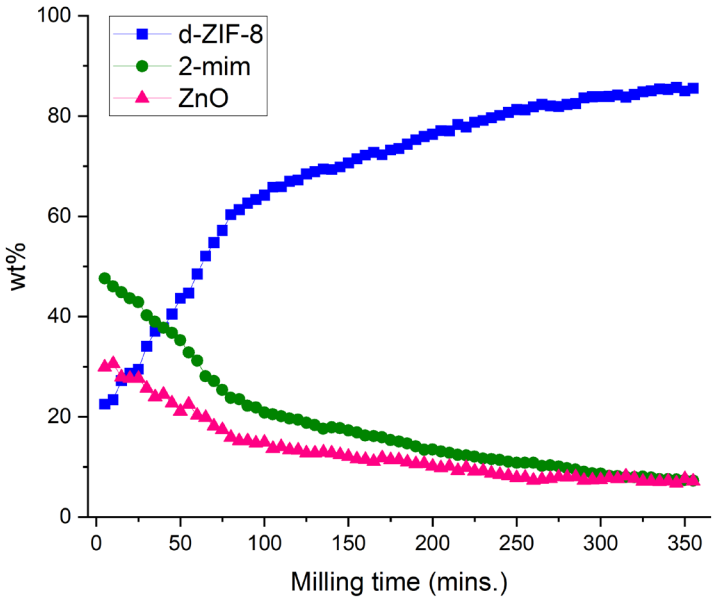

Figure 56. Quantitative analysis, obtained from Rietveld multiphase refinement, for the *in-situ* reaction showing the consumption of 2-methylimidazole and ZnO starting reactants, while the target product ZIF-8 is formed.

Discussion and future outlook

The development and evaluation of a ball-mill reactor compatible with *in-situ* neutron diffraction on GEM represent a substantial advance in mechanochemical methodology. The systematic characterisation of reactor materials demonstrated that neutron transparency and background behaviour vary dramatically across designs, with vanadium emerging as the only material that provides a truly unobstructed diffraction window. As shown in the collected GEM data, vanadium reactors and milling balls produce no detectable Bragg reflections and only a nearly flat background, enabling full visibility of sample-derived features. This establishes vanadium as the benchmark material for future *in-situ* mechanochemical studies, despite the practical challenges associated with machining bespoke vanadium components.

The aluminium-based cylindrical design offered a favourable compromise between manufacturability, mechanical robustness and diffraction quality. Aluminium reactors exhibited lower background levels than PTFE, ZrO_2 or stainless steel, and their reflections were sufficiently spaced to leave usable low-d-spacing regions for sample analysis. These characteristics make aluminium a viable option for reactions where vanadium is impractical, particularly for exploratory or off-beamline optimisation work. In contrast, PTFE reactors, while attractive due to their low crystallinity, suffered from high background scattering and mechanical deformation under prolonged milling, limiting their long-term applicability. The leakage issues observed in early PTFE designs further emphasise the importance of reliable sealing strategies, especially for liquid-assisted grinding and air-sensitive reactions.

The neutron-diffraction tests also confirmed that ancillary components—such as the aluminium safety pot and the application of vacuum in the GEM tank—do not inherently compromise data quality when properly aligned and operated. This is essential for safe and routine deployment of the reactor on GEM. The ability to maintain acceptable diffraction quality under ambient conditions simplifies experimental logistics and broadens the range of feasible mechanochemical studies.

The *in-situ* mechanosynthesis trials demonstrated that the reactor can successfully capture real-time structural evolution during milling. Even in cases where reactions did not reach full completion, the diffraction data clearly revealed phase consumption and product formation, validating the reactor's capability for kinetic and mechanistic studies. The observation that some reactions proceed rapidly—showing product formation within minutes—highlights the importance of continuous, uninterrupted data collection, which this reactor now enables. The absence of detectable intermediates in the sequential Rietveld refinements suggests either a direct reaction pathway or intermediates too short-lived to be captured by conventional stop-and-sample approaches, underscoring the value of true *in-situ* monitoring.

Looking ahead, several avenues for further development are evident. First, expanding the use of vanadium—both for reactor bodies and milling media—would maximise diffraction quality and enable more complex mechanistic investigations, including reactions involving weakly scattering intermediates. Second, refining the cylindrical aluminium design, potentially incorporating thinner walls or composite structures (null scattering alloy materials), could further reduce background while maintaining mechanical stability. Third, integrating controlled-atmosphere capabilities, such as indium-sealed vanadium reactors, will open the door to studying air-sensitive systems including hydrides, nitrides and metastable phases.

Finally, the successful deployment of this reactor on GEM establishes a platform for future mechanochemical research at neutron facilities. With reliable *in-situ* capability now demonstrated, the next steps include systematic kinetic studies, exploration of solvent-free reaction pathways, and the investigation of mechanochemical processes that have remained inaccessible due to the limitations of *ex-situ* sampling. The reactor developed in this project provides the foundation for these advances, positioning neutron diffraction as a powerful tool for uncovering the fundamental mechanisms that govern mechanochemical transformations.

References

[1] J.-L. Do and T. Friščić, 'Mechanochemistry: A Force of Synthesis', *ACS Cent. Sci.* (2017) **3**, 13–19. DOI: 10.1021/acscentsci.6b00277.

[2] G. A. A. Bazedi, A. E. Al-Rawajfeh, M. A. Abdel-Fatah, M. R. Alrbaihat and E. AlShamaileh, in 'Handbook of Greener Synthesis of Nanomaterials and Compounds', Elsevier (2021), pp. 405–418.

[3] M.-L. Tong and X.-M. Chen, in 'Modern Inorganic Synthetic Chemistry', Elsevier (2017), pp. 189–217.

[4] A. A. L. Michalchuk and F. Emmerling, 'Time-Resolved In Situ Monitoring of Mechanochemical Reactions', *Angew. Chemie Int. Ed.* (2022) **61**, 21. DOI:10.1002/anie.202117270.

[5] A. C. Hannon, 'Results on disordered materials from the GEneral Materials diffractometer, GEM, at ISIS', *Nuclear Instruments and Methods in Physics Research A* (2005) **551**, 88–107. DOI:10.1016/j.nima.2005.07.053.

[6] A. A. Coelho, 'TOPAS and TOPAS-Academic: an optimization program integrating computer algebra and crystallographic objects written in C++', *J. Appl. Cryst.* (2018) **51**, 210-218. https://topas-academic.com/, DOI:10.1107/S1600576718000183.

[7] J. Beamish-Cook, K. Shankland, C. A. Murray, P. Vaqueiro, 'Insights into the Mechanochemical Synthesis of MOF-74', *Cryst. Growth Des.* (2021) **21**, 3047-3055. DOI: 10.1021/acs.cgd.1c00213.